Research Square

Preprints are preliminary reports that have not undergone peer review.
They should not be considered conclusive, used to inform clinical practice,
or referenced by the media as validated information.

Glabranin counteracts MAFLD by stimulating liver lipid catabolism via the PKA-AMPK axis

Hind Moukham
University of Milano-Bicocca
Giorgia Spandri
University of Milano-Bicocca
Daniela Beghelli
Università di Camerino
Valentina Santoro
University of Salerno
Simona Serio
University of Salerno
Anna Lisa Piccinelli
University of Salerno
Elisa Maffioli
University of Milan
Gabriella Tedeschi
University of Milan
Massimo Labra
University of Milano-Bicocca
Bianca Schrul
Saarland University
Farida Tripodi
University of Milano-Bicocca
Paola Coccetti
paola.coccetti@unimib.it

University of Milano-Bicocca

Research Article

Keywords: Lipid droplets, natural compounds, lipolysis, autophagy, Drosophila melanogaster

Posted Date: November 9th, 2026

DOI: https://doi.org/10.21203/rs.3.rs-11346624/v1

License: This work is licensed under a Creative Commons Attribution 4.0 International License.
Read Full License

Additional Declarations: No competing interests reported.

Glabranin counteracts MAFLD by stimulating liver lipid catabolism via the PKA-AMPK axis

Hind Moukham[1], Giorgia Spandri[1], Daniela Beghelli[2], Valentina Santoro[3,4], Simona Serio[3,4], Anna Lisa Piccinelli[3,4], Elisa Maffioli[5], Gabriella Tedeschi[5], Massimo Labra[1,3], Bianca Schrul[6,7], Farida Tripodi[1,3], Paola Coccetti[1,3*]

[1]Department of Biotechnology and Biosciences, University of Milano-Bicocca, Milano, Italy.

[2]School of Biosciences and Veterinary Medicine, University of Camerino, Camerino (MC), Italy.

[3]National Biodiversity Future Center (NBFC), Palermo, Italy.

[4]Department of Pharmacy, University of Salerno, Fisciano, Italy.

[5]DIVAS, Department of Veterinary Medicine and Animal Sciences, University of Milano, Milano, Italy.

[6]Medical Biochemistry and Molecular Biology, Center for Molecular Signaling (PZMS), Faculty of Medicine, Saarland University, Homburg, Germany.

[7]Center for Biophysics, Saarland University, Homburg, Germany.

*corresponding author: paola.coccetti@unimib.it

ABSTRACT

Background: Metabolic dysfunction-associated fatty liver disease (MAFLD) is the most prevalent chronic liver disorder worldwide and remains without effective pharmacological interventions capable of targeting the underlying metabolic dysfunction. Here, we investigated the therapeutic potential and molecular mechanisms of action of glabranin, a prenylated flavanone isolated from *Glycyrrhiza glabra* leaves, in complementary *in vitro* and *in vivo* models of steatosis.

Methods: Steatosis was induced in HepG2 cells by exposure to oleic and palmitic acids, and in *Drosophila melanogaster* through high-fat diet feeding. The effects of

glabranin on lipid droplets accumulation and metabolic homeostasis were evaluated using integrated phenotypic, proteomic, and kinome analyses.

Results: Glabranin markedly reduced intracellular lipid droplets accumulation in oleic/palmitic acid-overloaded HepG2 cells, as well as in Huh7 cells. Integrated proteomic and kinome profiling revealed robust activation of the cAMP-PKA-AMPK signaling axis, accompanied by coordinated induction of lipid-catabolic pathways. Mechanistically, glabranin enhanced lipolysis and lipophagy, promoted mitochondrial β-oxidation, and stimulated NRF2-dependent antioxidant responses, thereby restoring metabolic flexibility and reducing lipotoxic stress. The metabolic benefits of glabranin were confirmed in *vivo* using a high-fat diet-induced *D. melanogaster* model. Glabranin supplementation significantly decreased lipid accumulation, restored locomotor performance, and improved survival, demonstrating efficacy across evolutionarily conserved metabolic pathways.

Conclusions: Our findings identify glabranin as a previously unrecognized metabolic modulator that reprograms hepatic lipid metabolism through activation of the cAMP-PKA-AMPK network. By simultaneously enhancing lipid droplets clearance, mitochondrial fatty acid utilization, and antioxidant defense, glabranin effectively counteracts steatotic state in both *in vitro* and *in vivo* models. These results position glabranin as a promising candidate for the prevention and treatment of early-stage MAFLD and provide a strong rationale for its further preclinical development.

Keywords: Lipid droplets; natural compounds; lipolysis, autophagy; *Drosophila melanogaster*

Background

Metabolic dysfunction-associated fatty liver disease (MAFLD), also known as non-alcoholic fatty liver disease (NAFLD), is the most prevalent chronic liver disorder worldwide, affecting approximately 25% of the global population [1,2]. MAFLD encompasses a broad pathological spectrum, ranging from simple steatosis to non-alcoholic steatohepatitis (NASH), now called metabolic dysfunction-associated

steatohepatitis (MASH), fibrosis, cirrhosis, and eventually hepatocellular carcinoma [3]. A crucial aspect of MAFLD is that early-stage hepatic steatosis is reversible if treated before the development of significant inflammation or fibrosis. Several clinical studies demonstrate that moderate weight loss through lifestyle interventions such as diet and exercise can lead to the complete resolution of steatosis and marked improvements in liver histology [4].

Conversely, excessive lipid accumulation in hepatocytes enhances the synthesis of lipid droplets (LDs) in the endoplasmic reticulum (ER) and increases lipid peroxidation, thereby amplifying oxidative stress and triggering inflammatory responses [5]. Consequently, limiting hepatic lipid overload remains a challenging yet critical therapeutic strategy for MAFLD, particularly in the context of redox dysregulation [6]. The transcription factor NRF2 (Nuclear factor erythroid 2-related factor 2) plays a pivotal role in cellular defence mechanisms mitigating lipid peroxidation and protecting hepatocytes from oxidative stress [7], participating also in the regulation of hepatic steatosis during the progression of MAFLD [8].

Lipolysis and lipophagy are two essential and interconnected pathways responsible for maintaining hepatic lipid homeostasis. Cytosolic lipolysis involves the enzymatic hydrolysis of stored neutral lipids (mainly triglycerides, TGs) within LDs; in parallel, lipophagy mediates the degradation of LDs through lysosomal delivery, contributing significantly to hepatic lipid clearance [9]. Importantly, these two processes act in a coordinated manner rather than independently. Lipolysis, primarily controlled by protein kinase PKA, reduces the size of large LDs, facilitating their subsequent recognition and autophagic engulfment by lipophagy [10]. The free fatty acids generated by these complementary processes are ultimately transported into mitochondria, where they undergo β-oxidation to produce acetyl-CoA and ATP, providing energy and preventing lipotoxicity [11]. Dysregulation of either pathway contributes to excessive LDs accumulation, impaired mitochondrial β-oxidation and the progression of MAFLD. Remarkably, mouse studies show that NRF2 deficiency increases susceptibility to diet-induced NASH, with enhanced steatosis driven by upregulated lipogenesis, suppressed β-oxidation along with basal UPR dysregulation, promoting lipid accumulation and worsening pathology [12].

Another important regulator of lipid metabolism is AMP-activated protein kinase (AMPK). AMPK activation is primarily mediated by Liver Kinase B1 (LKB1), a principal upstream kinase which regulates cellular energy homeostasis. Once activated, AMPK promotes autophagy to stimulate lipid catabolism. In parallel, it inhibits acetyl-CoA carboxylase 1 (ACC1), resulting in reduced *de novo* lipogenesis [13], as well as ACC2, promoting mitochondrial β-oxidation of fatty acids [14]. Dysregulation of this pathway contributes to lipid accumulation, mitochondrial dysfunction, and oxidative stress, key factors accelerating MAFLD progression [15]. Indeed, the down-regulation of this kinase is closely linked to endoplasmic reticulum (ER) stress and hepatic steatosis [16]. Collectively, clinical investigations and experimental studies consistently demonstrate that lipid toxicity and oxidative stress are closely associated with the development and progression of MAFLD [17].

Current pharmacological options for MAFLD include pioglitazone, GLP-1 receptor agonists, and vitamin E, which have demonstrated reduced steatosis and inflammation [3,18,19]. Moreover, natural-derived bioactive compounds are emerging as promising candidates due to their ability to modulate oxidative stress, attenuate lipid peroxidation, and restore redox homeostasis [6,20,21]. For instance, different polyphenols, terpenoids, alkaloids, as well as natural extracts have the ability to activate AMPK and modulate lipid metabolism in MAFLD models (for reviews see [22,23]). Within this context, *Glycyrrhiza glabra*, from which liquorice is obtained, represents a promising source of bioactive molecules, due to its prenylated flavonoids and polyphenolic compounds with reported antioxidant and anti-inflammatory properties [24,25]. Furthermore, *G. glabra* leaves represent a by-product of the food industry, since only roots are used to produce liquorice and the valorization of this biomass could support the economic value of licorice cultivation. In this study, we investigated the effects of a bioactive compound of *G. glabra* leaves, the prenylated flavanone glabranin, on lipid metabolism using fatty acid induced steatotic *in vitro and in vivo* models.

Methods

Preparation of *G. glabra* extract and purification of main compounds

G. glabra leaves were harvested in July 2024, during the flowering stage, from 3/4-year-old plants cultivated in Castrolibero, a typical Calabrian licorice production area. Flavanone-rich extracts from *G. glabra* leaves were obtained by supercritical CO_2 extraction (SFE-CO_2) performed in static (20 min) e dynamic (30 min) modes at 40 °C and 370 bar using a Spe-ed Helix system (Applied Separations, Allentown, PA, USA) as described in [25]. Extractions were carried out in triplicate, and the resulting extracts were pooled after quality control by quantitative UHPLC-UV analysis at 290 nm, according to [25]. The extract contained 6.0 ± 0.4, 8.2 ± 0.8 and 22.0 ± 0.9 g 100 g^{-1} of glabranin, licoflavanone, and pinocembrin, respectively.

Glabranin, licoflavanone e pinocembrin were isolated from the extract using a Biotage Selekt automated flash chromatography system (Biotage Sweden AB, Uppsala, Sweden). Extract aliquots (500 mg), dissolved in 1 mL of aqueous ethanol (75 % *v*/v), were loaded onto a Biotage Sfär C18 D column (100 Å, 30 µm, 12 g) and fractionated using a gradient of water (A) and methanol (B) at a flow rate of 12 mL min^{-1} as follows: 15 column volume (CV), 60 % B; 1 CV, 60–82 % B; 9 CV, 82–82 % B; 6 CV, 82–95 % B). UV spectra were monitored in the 200-400 nm range, and the collected wavelength was set at 290, using a threshold of 100 mAU. Fractions containing the target compounds were pooled and further purified on a Biotage Sfär C18 D column (100 Å, 30 µm, 6 g) under the same conditions. Purified compounds were identified using NMR and HRMS analyses [26]. The purity of the isolated compounds (>95%) was assessed by HPLC-PDA analysis.

Cell cultures

HepG2 cells were obtained from ATCC. Huh7 liver cancer cells were provided by the Japanese Collection of Research Bioresources (JCRB) Cell Bank. Cell cultures were regularly tested for Mycoplasma contamination using the Mycoblue Mycoplasma detector (Vazyme). Cells were cultured in RPMI-1640 medium supplemented with 10% (v/v) FBS, 2 mM L-glutamine, 100 U/mL penicillin, and 100 µg/mL streptomycin. Cells were maintained at 37 °C in a humidified 5% CO_2 incubator. To induce steatosis *in vitro*, cells were treated for 24 h (unless otherwise specified) with oleic acid and palmitic acid (2:1) at a total concentration of 1 mM (OP), prepared in culture medium supplemented with 1% bovine serum albumin (BSA) for 24 h. For co-treatment conditions, cells were simultaneously incubated with the 1 mM OP mixture and either

the *G. glabra* extract, or glabranin or licoflavanone or pinocembrin at the indicated concentration dissolved in ethanol (200x stock solutions). Control cultures were treated with the corresponding vehicle volumes, consisting of both 1% BSA and ethanol, ensuring identical solvent exposure across all four experimental groups. Compound C, H89, Bafilomycin A were dissolved in DMSO and used at the indicated concentrations.

Cell kinome profiling

Cells were washed and lysed in M-PER lysis buffer (Thermo Fisher Scientific), supplemented with 150 mM NaCl and Halt Protease and Phosphatase inhibitors (Thermo Fisher Scientific), following PamGene's instructions. The lysates were centrifuged at 4 °C for 15 min at 10,000 × g, and the supernatants were stored at -80 °C until further analysis. Kinome profiling was conducted using the PamStation® 12 platform at the ProMeFa facility in San Raffaele Hospital, Milan (Italy), enabling high-throughput profiling of composite kinase activities. The PamGene assays measure kinase activity in cell lysates by evaluating the phosphorylation of peptides, which are kinase targets/substrates that are immobilized on the PamChip® microarrays (196 protein tyrosine kinase (PTK) and 144 serine/threonine kinase (STK) phosphosites). STK and PTK microarray assays were performed according to the manufacturer's instructions. Briefly, cell lysates (2 µg for STK, 5 µg for PTK) were mixed with reaction solutions and placed on STK PamChips and PTK PamChips (PamGene). Biological triplicates of the cell lysates were processed within the same assay run to allow for correct comparisons. The data workflow consisting of image quantification, quality control, statistical analysis, visualization, and interpretation was performed using BioNavigator® software (BN63; PamGene® International, The Netherlands). The ratios of the normalized signals of the treated samples and controls were used to calculate the log-fold change for each peptide. Statistical significance was tested using unpaired t-tests, and the results are represented by volcano plots generated using BN63. Peptides with a p-value < 0.05 were considered a significant change in the degree of phosphorylation of a peptide in the comparison groups. Enrichment analysis was performed using EnrichR [27] on regulated kinases, according to the KEGG pathway database.

Analysis of glabranin availability in cells

To evaluate the intracellular/cell-associated level of glabranin, $7x10^5$ HepG2 cells were seeded in 60-mm dishes and treated with 9.2 µM glabranin up to 24 h. For metabolite extraction, cells were washed twice with PBS before being lysed with ice cold 80% methanol solution for 5 min. The lysate was transferred into a 1.5 mL tube and sonicated in a water bath, 1 min on and 1 min off for 5 times. Samples were centrifuged at 14,000 x g for 30 min at 4 °C and the supernatant was filtered using a 3 kDa molecular weight cut-off filter at 14,000 x g for 1 h at 4 °C. The eluate was transferred in LC-MS vials and stored at -20 °C. Samples were injected into a Xevo G2-XS quadrupole time of flight mass spectrometer coupled to a Waters ACQUITY ultra-performance liquid chromatography (UPLC) H-Class system through an ESI source (Waters Corporation, Milford, MA, USA). The instrument was operated in positive ion current in sensitivity mode. The capillary voltage was maintained at 1.5 kV with the source temperature held constant at 140 °C. An ACQUITY UPLC® BEH C18 1.7 µm, 2.1mm x 50mm, (Waters Corporation, Milford, MA, USA) was used for analyte separation. The flow rate was set to 400 µL/min with a column temperature of 40 °C. A gradient of solvent A (99.9% LC-MS-grade water with 0.1% formic acid) and solvent B (LC-MS-grade 99.9% acetonitrile with 0.1% formic acid) was applied with a total run time of 12 min as follows: 0-0.3 min at 2% B; 0.3-6.3 min linear increase from 2 to 98% B; 6.3-8.3 98%B; 9-12 min 2% B. Transition selection and optimization of collision energy were performed manually on glabranin solution, and data acquisition in MRM mode was performed with Masslynx (v4.2). The transitions monitored were m/z 325.15 (CE20V) → m/z 269.08 (quantifier) and 325.15 (CE 28V) → m/z 165.02 (qualifier). Analyte quantity was extrapolated from the standard curve, 156-1250 nM of the analyte (R^2 =0.993). The accuracy of each standard point was calculated with TargetLynx based on the determined linear regression curve and should be between 80% and 120% of the expected value.

Cell viability assay

Cell viability was determined using the MTT (3-[4,5-dimethylthiazol-2-yl]-2,5 diphenyltetrazolium bromide) assay. $9x10^3$ HepG2 cells were seeded in a 96-well plate and treated for 24 h, then the culture medium was removed and cells were incubated for 2 h at 37 °C in 100 µL of medium containing 0.5 mg/mL MTT. Finally, 100 µL of solubilization buffer (10% Triton X-100, 0.1 N HCl in isopropanol) was added to cells.

Absorbance was measured using a microplate reader (BioTek Synergy H1, Agilent) at 570 nm.

Cell shotgun mass spectrometry analysis

HepG2 cells under four different conditions (CNT, GLA, OP, OP+GLA) were analyzed by a shotgun label-free proteomic approach for the identification and quantification of expressed proteins. Cell lysis was performed in a urea lysis buffer containing 20 mM HEPES pH 8.0, 8 M urea, proteases and phosphatase inhibitor cocktails. The homogenate was sonicated using an ultrasonic probe in bursts of 30 s and centrifuged at 21,400 × g for 15 min at 18 °C to pellet the cell debris [28]. Prior to proteolysis, proteins were reduced with 13 mM dithiothreitol (15 min at 50 °C) and alkylated with 26 mM iodoacetamide (30 min at room temperature). The material was diluted to a final concentration of 1 M urea by addition of 20 mM HEPES, pH 8.0 and digested overnight with sequencing-grade trypsin (Sigma-Aldrich) for 16 h at 37 °C using a protein:enzyme ratio of 20:1 in the presence of 1 mM methylamine. The collected peptides were desalted using Zip-Tip C18 before MS analysis as reported in [29]. NanoHPLC coupled to MS/MS analysis was performed on Dionex UltiMate 3000 directly connected to a Q-Exactive Plus Orbitrap plus mass spectrometer (Thermo Fisher Scientific) by a nanoelectrospray ion source. Peptide mixtures were enriched on 75 µm ID × 150 mm EASY Spray PepMap RSLC C18 column (Thermo Fisher Scientific) and separated using the LC gradient: 1% acetonitrile (ACN) in 0.1% formic acid for 10 min, 1-5% ACN in 0.1% formic acid for 6 min, 5-38% ACN in 0.1% formic acid for 147 min and 38-63% ACN in 0.1% formic for 3 min at a flow rate of 0.3 µL/min. Orbitrap MS spectra of eluting peptides were collected over an m/z range of 375-1500 at resolution of 70,00, operating in a data-dependent MS2 mode of the 10 most intense peaks from full scan using an isolation window of 3 m/z and a normalized collision energy of 35. HCD MS/MS spectra were acquired in Orbitrap at the resolution of 17, 500. Dynamic exclusion was set to 30 s. Rejection of +1 and unassigned charge states were enabled.

A database search was conducted against the *Homo sapiens* Uniprot sequence database (release 22 September 2025) with MaxQuant (version 1.6.1.0) software. The initial maximum allowed mass deviation was set to 20 ppm for monoisotopic precursor ions and 0.5 Da for MS/MS peaks. Enzyme specificity was set to trypsin, defined as

C-terminal to Arg and Lys excluding Pro, and a maximum of two missed cleavages were allowed [30]. Carbamidomethylcysteine was set as a fixed modification, while Met oxidation and Asn/Gln deamidation were set as variable modifications. Quantification in MaxQuant was performed using the built-in label free quantification algorithms (LFQ) based on extracted ion intensity of precursor ions. False protein identifications (1%) were estimated by searching MS/MS spectra against the corresponding reversed-sequence (decoy) database.

Statistical analysis of Max Quant results was performed using the Perseus software (version 1.6.1.4). Principal component analysis-based multiconfidence ellipse analysis, PCA, was carried out on quantitative data related to proteins expressed at the four different conditions using the SRplot web tool (https://www.bioinformatics.com.cn/srplot). Only proteins present and quantified in at least 75% of the repeats were positively identified in a sample and used for statistical analysis.

Focusing on specific comparisons (GLA *vs* CNT, OP *vs* CNT and OP+GLA *vs* OP), proteins were considered differentially expressed if they were present only in one condition or showed significant t-test difference (Student's t-test p-value ≤ 0.05). Bioinformatic analyses were carried out by Panther (release 19.0) [31] and GSEA (release 4.3.2) to cluster enriched annotation groups of molecular pathways (Reactome) and networks within the set of identified proteins. Functional grouping was based on the Fisher's exact test FDR ≤ 0.05 and at least 3 counts.

Interaction networks were visualized using the "Search Tool for Recurring Instances of Neighbouring Genes" (STRING 12.0 release July 26, 2023) [32], setting the minimum required interaction score at 0.4 and hiding disconnected nodes.

Western blot analysis

Cells were lysed in RIPA buffer (Thermo Scientific) supplemented with protease inhibitors (Roche) and phosphatase inhibitor cocktails (Merck). After that, lysates were centrifuged 10 min at 18,000 x g at 4 °C, and the supernatants were collected. Protein concentration was determined using the Bradford assay (Bio-Rad). Protein samples were separated by Tris-glycine SDS-PAGE and transferred to 0.22 µm nitrocellulose membranes using the Trans-Blot Turbo (Bio-Rad). After the transfer, the membranes

were blocked with 5% non-fat dry milk and primary antibodies anti-pT172-AMPK (#2535, 1:1000, Cell Signaling Technology), anti-AMPKα (#2532, 1:100, Cell Signaling Technology), anti-pS79-ACC1 (#3661, 1:500, Cell Signaling Technology), anti-ACC1 (#3662, 1:500, Cell Signaling Technology), anti-pS563-HSL (PA5-17488, 1:1000, Invitrogen), anti-pS660-HSL (PA5-64494, 1:1000, Invitrogen), anti-HSL (PA5-17196, 1:1000, Invitrogen), anti-LC3 (14600-1-1AP, 1:1000, Proteintech), anti-pS428-LKB1 (#C67A3 1:1000, Cell Signaling Technology), anti-LKB1 (#3047, 1:1000, Cell signaling Technology), anti-NRF2 (PA5-27882, 1:1000, Invitrogen), anti-phospho-PKA-substrate (RRXS*/T*, #9624, 1:1000, Cell Signaling), anti-PLIN2 (SAb4200452, 1:1000, Merck), anti-pT389-S6K (144-50737-100, 1:1000, Reybiotech), anti-S6K (#2212, 1:1000, Cell Signaling), anti-pS1387-TSC2 (AP1117, 1:1000, ABclonal), anti-TSC2 (FNab09101, 1:1000, FineTest), anti-vinculin (V9131, 1:5000, Merck) were used. Conjugated secondary antibodies, either HRP conjugated (Cell Signaling Technology) or fluorophore conjugated (IRDye 680LT Goat, from Licor Biosciences) were applied. For chemiluminescent detection, signals were revealed using enhanced chemiluminescence (ECL) reagents and captured using the ChemiDoc system (Bio-Rad). Fluorescent signals were directly acquired using the Odyssey CLx imager (LICORbio). When necessary, membranes were stripped with 0.2 M Gly, 0.5 M NaCl, pH 2.8, and reprobed with other antibodies. The intensity of protein bands was quantified using ImageLab and Image Studio v6.2 softwares.

Cell BODIPY staining and immunofluorescence assays

For the visualization and quantification of LDs, cells were grown on glass coverslips pre-treated with 0.01% poly-L-lysine to ensure optimal cell adhesion. Cells were washed twice with Phosphate-Buffered Saline (PBS) and fixed with 4% formaldehyde solution for 15 min at room temperature. Following fixation, cells were washed again with PBS and stained with 0.05 µg/mL BODIPY 493/503 (Invitrogen) for 30 min or HCS LipidTOX Green (1:2000, Invitrogen) at 37°C in the dark. Coverslips were then washed twice, and mounted onto glass slides using a mounting medium containing DAPI (4',6-diamidino-2-phenylindole) for nuclear counterstaining. For the quantification of LDs including the average number and volume per cell, image analysis was performed using Cell-ACDC software. Specifically, the segmentation of individual LDs was carried out via automatic thresholding per cell, which allows for robust and unbiased isolation of the LD signal from the background and accurate delineation of the

boundaries of each single droplet. This automated method ensured precise quantification of both the average number of LDs per cell and the average volume of LDs per cell across all experimental conditions.

For immunofluorescence experiments, cells grown on coverslips pretreated with poly-L-lysine were washed with PBS, fixed with 4% formaldehyde for 15 min, and permeabilized with PBS-0.05% Triton X-100 for 10 min. Then, cells were washed in blocking solution (PBS-1% BSA), blocked at room temperature for 60 min, and then incubated overnight at 4 °C with the primary antibody anti-NRF2 (PA5-27882, 1:200, Invitrogen), anti-LC3 (#2775, 1:300, Cell Signaling), or for 1 h at room temperature with anti-LAMP1 (PA1-654A. After that, cells were incubated with anti-rabbit IgG-CFL 488 (sc-516248, 1:200, Santa Cruz Biotechnology) or anti-rabbit Cy3 (1:500, #715-605-151, Jackson ImmunoResearch) secondary antibodies for 1 h and 30 min respectively. Coverslips were mounted with a DAPI-containing mounting medium or Hoechst 33342 (1:5000, Invitrogen) for nuclear staining. Image acquisition was performed using a THUNDER Imager (Leica Microsystems) and a confocal microscope (LSM 900, ZEISS). For colocalization analysis between LDs and Lysosomal-Associated Membrane Protein 1 (LAMP1), background subtraction was performed prior to signal quantification. Colocalization was measured by calculating Mander's overlap coefficients (tM1 and tM2) using costes-based automatic thresholding to account for channel-specific background noise and determine the fractional overlap between signals, on a single Z-stack optical section per field of view. Consistent exposure settings were maintained across all experimental conditions for comparative analysis.

FAO blue measurement

To evaluate the rate of fatty acid oxidation (FAO), HepG2 cells were seeded in 12-well black-walled plates at a density of 2.4 x 10^4 cells/well. After 24 h, cells were treated under steatotic conditions, in the presence or absence of 9.2 µM GLA or an equal volume of EtOH as vehicle control. Following the 24 h treatment, the culture medium was removed and cells were washed twice with HEPES-buffered medium (pH 7.4) to remove exogenous fats and serum. Cells were then incubated for 2 h at 37°C with a cell-permeable coumarin-based palmitate derivative (FAOBlue, Funakoshi) at a final concentration of 40 µM in HEPES-buffered saline. This cell-permeable probe is

designed to emit blue fluorescence only upon metabolic processing by the mitochondrial β-oxidation pathway. Immediately after incubation, cells were washed again with HEPES-buffered medium to eliminate any non-internalized probe. Images were acquired using THUNDER Imager (Leica Microsystems) with a DAPI-compatible filter set (Excitation/Emission: 350/461 nm). Consistent exposure settings were maintained across all experimental conditions for comparative analysis.

cAMP measurement

cAMP was extracted in 0.1 N HCl from HepG2 cells grown in control conditions or treated with 9.2 µM GLA for 5 min. cAMP levels were measured using the cAMP (Cyclic Adenosine Monophosphate) ELISA Kit (NeoBiotech) following the manufacturer's instructions. In each well samples were normalized by protein content by using the Bradford assay.

Bioenergetics by Seahorse technology

Mitochondrial oxygen consumption rate (OCR) were determined by using Seahorse XFe96 Analyzer (Agilent Technologies). HepG2 cells were seeded in Agilent Seahorse cell culture microplates at a density of 2×10^4 cells/well. 24 h after seeding cells were left untreated (CNT), or treated with GLA, OP or OP+GLA for 24 h, and then analyzed by using the Seahorse XF Mitostress assay kit (Agilent Technologies), according to the manufacturer's instructions. Three measurements of OCR were taken for the baseline and after the sequential injection of mitochondrial inhibitors (1.5 µM oligomycin, 1.5 µM FCCP and 0.5 µM rotenone/antimycin A). OCR from each well were normalized by protein content by using the Bradford assay.

For palmitate FAO assay, HepG2 cells were seeded in Agilent Seahorse cell culture microplates at a density of 2×10^4 cells/well. 24 h after seeding the medium was replaced with RPMI-1640 limited medium, supplemented with 2 mM glucose, 1 mM glutamine, 0.5 mM L-carnitine and 1% FBS, in the absence or presence of GLA for 16 h. For the assay, the medium was exchanged with RPMI-1640 medium supplemented with 2 mM glucose, 0.5 mM L-carnitine and 150 µM palmitic acid/BSA or BSA alone. Whole-cell oxygen consumption was measured on an Agilent Seahorse XFe96 Analyzer. Three measurements of OCR were taken for the baseline and after the sequential injection of mitochondrial inhibitors (1.5 µM oligomycin, 1.5 µM FCCP and

0.5 µM rotenone/antimycin A). OCR from each well were normalized by protein content by using the Bradford assay.

In vivo assays in *Drosophila melanogaster*

The wild-type *Drosophila melanogaster* strain (w^{1118}) was obtained from the Bloomington Drosophila Stock Center (Indiana University, Bloomington, IN, USA) and used throughout the study.

Newly emerged males were collected within 24 h of eclosion from synchronized parental populations and maintained for one day on Formula 4-24® medium (control diet, CD; Carolina Biological, Burlington, NC, USA). The medium was supplemented with yeast pellets (*Saccharomyces cerevisiae*) in each culture tube and hydrated with sterile distilled water. Male flies (n=16 tubes, 25 flies per tube) were reared under controlled environmental conditions at 21 °C and 60% relative humidity, with a 12 h light-dark cycle. At one day of age, flies were subdivided into four experimental groups (n=4 tubes per group; 100 flies per group): CNT, GLA (glabranin treatment), fatty diet (FD; a high-lipid diet obtained by adding 30% (w/w) coconut oil), and FD+GLA. Glabranin was first dissolved in ethanol (EtOH) to prepare a 10 mM stock solution and then diluted in a 5% sucrose solution to a final concentration of 18 µM. After 1 h of exposure to the experimental diets, 1-day-old flies were transferred to empty tubes containing a paper disk at the bottom soaked with 400 µL of glabranin solution (for GLA and FD+GLA) or with 5% sucrose solution containing the same amount of EtOH used for stock preparation (for CNT and FD). After 5 h of treatment, flies were subjected to a climbing assay (T0) according to Madabattula et al. [33], and then transferred back onto CNT or FD. This procedure was repeated for three consecutive days, with a final climbing assay (T1) performed after the third day of treatment.

On day 4, flies (n=5 per group) were anesthetized on ice for fat body dissection.

To evaluate the effect of glabranin supplementation on survival under high-fat diet conditions, newly emerged male flies were collected within 24 h of eclosion and maintained under the same environmental conditions described above. Flies were maintained on the high-fat diet (FD) throughout the experiment and randomly assigned to two experimental groups, each distributed across five independent tubes: FD (n=50 flies) and FD+GLA (n=49 flies). In parallel, flies received either a 5% sucrose solution containing the same amount of EtOH used for stock preparation (FD group) or a 5% sucrose solution supplemented with glabranin (18 µM; FD+GLA group). The sucrose

solutions were supplied on filter paper strips attached to the tube plugs, providing continuous access to the respective solutions throughout the two-week experimental period. The filter paper strips and sucrose solutions were replaced daily. Survival was monitored twice weekly, and Kaplan-Meier survival curves were generated and compared using the log-rank (Mantel-Cox) test.

Adipose tissue staining in adult *Drosophila melanogaster*

The fat body is a key metabolic organ and represents a suitable model for investigating mechanisms underlying organismal metabolism and pathophysiological processes. In the present study, abdomens collected at T1 were processed according to the protocol described by Ott et al. [34]. Briefly, tissues were fixed in 4% paraformaldehyde and then stained with Alexa Fluor™ 488 phalloidin (Thermo Fisher Scientific) and DAPI (4′,6-diamidino-2-phenylindole dihydrochloride; Thermo Fisher Scientific) to visualize F-actin and nuclei, respectively, while Nile Red was used for lipid droplet (LD) staining. Image acquisition was performed using a Thunder fluorescence microscope (Leica Microsystems), maintaining consistent exposure settings across all experimental conditions to ensure a reliable comparative analysis. High-resolution Z-stack images were captured to encompass the entire volume of the fat body adipocytes, providing a detailed three-dimensional view of the tissue architecture. For the precise quantification of lipid droplets (LDs), image processing and morphometric analysis were conducted using the Cell-ACDC software. The analytical workflow relied on the Alexa Fluor™ 488 phalloidin signal to define cellular boundaries, ensuring that all subsequent measurements were normalized per single cell. Within these segmented boundaries, individual LDs were identified through the Nile Red signal, enabling the precise calculation of both the average number and volume of LDs per cell across all experimental groups.

Statistical analysis

All experiments with cell cultures were conducted in triplicate unless otherwise specified. Statistical analyses were performed using the two-tailed Student's t-test, with significance set at $p < 0.05$. For *Drosophila*, the climbing performance was quantified by calculating the area under the curve (AUC) of the cumulative percentage of flies reaching the predefined climbing height over the 120 s observation period. AUC values were calculated for each independent vial using the trapezoidal method. Since

the same vials were assessed at day 1 and day 3, AUC data were analyzed using a two-way repeated-measures ANOVA, with experimental group as the between-subject factor and time as the within-subject factor. Pairwise comparisons among experimental groups within each time point were performed using Tukey's multiple-comparisons test. Survival curves were generated using the Kaplan-Meier in OASIS 2 (Online Application for Survival Analysis 2), and differences between the FD and FD+GLA were assessed using the log-rank (Mantel–Cox) test. A p-value<0.05 was considered statistically significant.

Results

Glabranin from *G. glabra* extract reduced lipid droplets *in vitro*

We have recently developed a supercritical CO_2 fluid extraction (SFE-CO_2) process for the selective recovery of pinocembrin (PINO) and the prenylated flavanones licoflavanone (LICO) and glabranin (GLA) from *G. glabra* leaf-exudate (Fig. 1A), yielding high-purity (> 30% flavanones), solvent-free and ready-to-use enriched extracts [25].

With the aim of evaluating the potential role of this extract in a context of lipid dysmetabolism, we employed an *in vitro* steatosis model to investigate its effects on lipid droplet formation. HepG2 cells were supplemented with oleic acid and palmitic acid at a 2:1 ratio (OP, 1 mM total concentration) for 24 h, resulting in robust LDs accumulation, as previously reported [35] (Suppl. Fig. S1A). Co-treatment with 50 µg/mL of *G. glabra* leaf extract for 24 h, which showed no toxicity (Suppl. Fig. S1B), led to a marked reduction in the number and volume of intracellular LDs in steatotic conditions, as assessed by fluorescence microscopy of BODIPY-stained cells (Suppl. Fig. S1C-E).

Then, to evaluate the contribution of the major components of the extract, we purified the predominant constituents GLA, LICO and PINO (Fig. 1A) using an automated purification procedure. Each compound was independently tested under both basal and steatotic condition, at concentrations corresponding to their respective abundances in 50 µg/mL of *G. glabra* extract (*e.g.*, 9.2 µM for GLA, 12 µM for LICO, and 43 µM for PINO). Remarkably, co-treatment of HepG2 cells with fatty acids and

each of the three compounds reduced the number of LDs per cell, highlighting that they act as bioactive modulators of lipid metabolism with potential relevance for impaired lipid homeostasis (Fig. 1B-C). Notably, GLA treatment promoted a shift toward larger LDs under both basal and steatotic conditions (Fig. 1D), a remodeling pattern associated with reduced cellular lipotoxicity [36–38]. Since PINO has been well-characterized for its effects on lipid metabolism [39,40], we decided to focus our attention on the prenylated compounds GLA and LICO, which are known to have a high permeability and bioavailability [41]. Although LICO is structurally similar to GLA, previous research has focused more extensively on its anti-tumoral and anti-inflammatory potential [42,43]. Consequently, we directed our investigation toward GLA, as it remains a poorly characterized molecule specifically within the context of lipid metabolism.

GLA exhibited excellent tolerability up to 20 µM (Fig. 1E) and showed rapid cellular uptake, with intracellular signal detectable 15 min after treatment and steadily increasing over 24 h (Fig. 1F). Quantitative flow cytometry demonstrated that GLA robustly decreased the neutral lipids content (~20%) in steatotic HepG2 cells (Fig. 1G), confirming fluorescence imaging-based observations (Fig. 1B-C). This lipid-lowering effect was confirmed also in Huh7 hepatoma cells, which accumulate substantially more LDs than HepG2. In these cells, GLA treatment induced a comparable reduction in the number of LDs, while their volume increased only in control condition (Suppl. Fig. S2A-C).

These data establish GLA as a non-toxic, rapidly internalized compound capable of significantly mitigating lipid-droplet overload in hepatocyte models of steatosis.

Glabranin activates NRF2-mediated stress response

To decipher how GLA affects lipid storage mechanistically, the proteome of HepG2 cells in control condition (CNT) or treated with oleate and palmitate (OP) for 24 h was analyzed by a shotgun proteomic approach, in the absence or presence of co-treatment with 9.2 µM GLA. The comparative analysis of the proteomes across the four experimental conditions (CNT, GLA, OP, OP+GLA) revealed a substantial set of proteins uniquely expressed within each dataset (53 proteins in CNT, 59 in GLA, 12 in OP and 82 in OP+GLA) (Supplementary Fig. S3A). PCA analysis clearly indicated that supplementation with GLA exerted a marked proteomic impact in both control and

steatotic conditions (Supplementary Fig. S3B). To identify the potential patterns and networks induced, the differentially or exclusively expressed proteins in the pair comparisons GLA vs CNT, OP vs CNT and OP+GLA vs OP, were further analysed by PANTHER and Reactome. The results strongly suggest that co-treatment with oleate, palmitate and GLA triggered a pronounced cellular stress response, including activation of pathways typically associated with chemical and heat stress (Supplementary Table 1 and Fig. 2A). Indeed, many proteins involved are direct interactors of Nuclear factor erythroid 2-related factor 2 (NRF2), which controls detoxification and redox homeostasis [44] (Supplementary Fig. S3C, Supplementary Table 2). Among them, GCLM (Glutamate-Cysteine Ligase Modifier), which drives the first and rate-limiting step in the biosynthesis of glutathione, PRDX3 (Peroxiredoxin-3), the mitochondrial thioredoxin-dependent peroxide reductase, NQO1 (NAD(P)H:quinone oxidoreductase), several chaperones (DNAJB1, HSPA6, HSPA12A, HSPA14) and proteasomal proteins (PSMA2, PSMC5, PSMD5, PSME3). This is consistent with the recently reported activation of the NRF2-pathway by GLA in neuroblastoma cells [45]. In keeping with these proteomic data, in steatotic cells GLA treatment significantly increases both nuclear localization (Fig. 2B-C) and total NRF2 levels (Fig. 2D-E). This activation of the antioxidant machinery translated into a marked improvement in cell viability under hydrogen peroxide-induced oxidative stress in steatotic cells treated with GLA (Fig. 2F).

A subset of differentially expressed proteins (Supplementary Table S1) clustered within anti-lipid peroxidation pathways, suggesting activation of a targeted cytoprotective program. In line with this signature, GLA suppressed lipid peroxidation, as quantified by C11-BODIPY oxidation, consistent with a direct mitigation of lipid peroxidation arising from fatty acid excess. Remarkably, this protective effect was NRF2-dependent, as pharmacological inhibition of NRF2 using ML385 abolishes the GLA effect on lipid peroxidation (Fig. 2G). This is consistent with the observed shift toward fewer but larger LDs (Fig. 1C,D). Indeed, esterification of vulnerable fatty acids into neutral lipid droplets, such as TAGs and sterol esters serves as an adaptive mechanism that shields lipids from oxidative damage and limits lipid peroxidation [46].

Altogether, these data position GLA as a bioactive compound that attenuates oxidative injury and lipid peroxidation, potentially counteracting molecular processes that sustain MAFLD progression.

Glabranin activates lipid catabolic pathways

To gain deeper insight into the molecular mechanisms underlying the effects of GLA on lipid metabolism, the PamGene technology was used to monitor alterations in the cellular kinome (https://pamgene.com/). Pathway enrichment analysis showed that GLA treatment altered the phosphorylation of 15 PTK peptides (targets of tyrosine kinases) and 20 STK peptides (targets of serine/threonine kinases) compared with control cells, whereas under steatotic conditions it induced changes in the phosphorylation of 7 PTK and 9 STK peptides (Suppl. Fig. S4A,B). Specifically, the kinase activities upregulated by GLA treatment both in control and steatotic conditions were: the focal adhesion kinase or Protein Tyrosine Kinase 2, encoded by PTK2, the Fibroblast Growth Factor Receptor 4 (FGFR4), the Protein kinase A catalytic subunit (PRKACA) and its homolog Protein kinase X-linked (PRKX), the cGMP-dependent protein kinases (PRKG1 and PRKG2), and Ribosomal Protein S6 Kinase A5 (RPS6KA5) (Suppl. Fig. S4C). Remarkably, all kinases stimulated by GLA were strongly connected to PKA, as suggested by the STRING analysis (Suppl. Fig. S4D,E, PRKACA and PRKACB marked in red). In addition, pathway analysis performed with EnrichR [27] revealed that several of the modulated kinases were associated with processes related to lipid metabolism, according to the KEGG pathway database (Fig. 2H,I). Under basal conditions, GLA amplified the lipolytic program. In steatotic cells, it engaged a broader metabolic repertoire, activating kinases involved in lipolysis, autophagy, and thermogenesis, the latter tightly coupled to degradative lipid metabolism and indicative of a catabolic shift (Fig. 2H,I).

In conclusion, integrated findings from both the proteomic and kinome assays indicate that GLA orchestrates a concerted activation of catabolic programs, suggesting that GLA stimulates the metabolic fluxes required to sustain efficient lipid clearance.

Glabranin stimulates PKA-mediated lipolysis

Since the molecular signature above reported pointed to the engagement of signaling nodes governing lipolysis (Fig. 2H,I) with PKA activity upregulated upon GLA treatment (Suppl. Fig. S4C-E), we next examined whether GLA effectively triggers a functional activation of PKA-dependent lipolysis. The lipolytic machinery is an integral

and complex system within lipid metabolism, and is largely regulated by β-adrenergic activation of the cAMP/PKA pathway, leading to phosphorylation of the lipases, as well as members of the perilipin family of coat proteins that regulate the access of lipases and other regulatory cofactors to LDs (Fig. 3A) [47]. To clarify this mechanism, we first quantified intracellular cAMP, the principal upstream activator of PKA [48]. Remarkably, GLA treatment caused a rapid rise in cAMP levels within 5 minutes (Fig. 3B), which closely paralleled the strong increase in PKA-substrate phosphorylation (pPKA substrates) (Fig. 3C,D). Notably, pharmacological inhibition of PKA using H89 in steatotic HepG2 cells treated with GLA led to a significant increase in the number of LDs per cell (Fig. 3E,F), accompanied by an increase of LDs volume (Fig. 3G). Given that active lipolysis preferentially targets larger lipid droplets for enzymatic breakdown [47], blocking PKA signaling prevents this cleavage process, causing intact LDs to accumulate and expand further. These findings indicate that PKA activity is required for GLA-induced LD mobilization.

The activation of the cAMP/PKA signaling by GLA prompted us to examine the phosphorylation of one of its downstream effectors, the hormone sensitive lipase HSL, at two regulatory sites. While phosphorylation of HSL-Ser563 remained unchanged upon GLA treatment under fatty-acid excess (Fig. 3H,I), GLA robustly increased phosphorylation at HSL-Ser660 in both basal and steatotic conditions (Fig. 3H,J), a modification known to promote HSL translocation to the LD surface and enhance lipolytic activity [49]. Consistently, although PLIN2 was markedly elevated in steatotic cells, GLA co-treatment effectively reduced PLIN2 level (Fig. 3K, L), thereby facilitating lipase access to LDs and promoting lipid mobilization [50]. This removal of the LD protective coat correlated with a significant increase in glycerol release after 24h-GLA treatment, in both steatotic HepG2 and Huh7 cells (Fig. 3M).

Together, these findings indicate that GLA activates PKA-dependent lipolysis in steatotic conditions.

Glabranin stimulates lipophagy through the activation of PKA-LKB1-AMPK signaling

To delineate the mechanisms downstream of PKA activation, we focused on the canonical PKA-LKB1-AMPK signaling axis [51]. LKB1 functions as the principal upstream kinase required for AMPK activation [52], positioning it as a critical node linking PKA signaling to AMPK-dependent metabolic regulation. Remarkably, 24h-GLA treatment enhanced LKB1 phosphorylation at Ser428 (Fig. 4A,C), a PKA-dependent phosphorylation site [52], and stimulated AMPK signaling in HepG2 cells, as observed by the increased phosphorylation of both AMPK and its target ACC1 (Fig. 4B, D,E).

Given the pivotal role of AMPK in regulating the autophagic pathway, we next investigated its functional involvement in GLA-mediated lipid clearance. To evaluate whether GLA engages the autophagic machinery, as already suggested by our multi-omic datasets (Fig. 2I, Suppl. Fig. S3D, and Suppl. Table S1), we investigated the autophagic flux markers, by quantifying both the LC3II/I ratio by western blot (Fig. 4F,G) and LC3 puncta by immunofluorescence following a 6 h exposure to fatty acids and GLA (Fig. 4H, I). Under basal conditions, GLA induced an increase in LC3 puncta per cell (Fig. 4H, I) without substantially altering the LC3-II/I ratio (Fig. 4F,G), a pattern that could indicate either enhanced autophagosome formation or downstream retention. In contrast, under palmitate/oleate loading, GLA induced a marked reduction in both the LC3-II/I ratio (Fig. 4F,G) and total LC3 puncta (Fig. 4H,I), potentially reflecting an accelerated autophagic turnover and clearance under lipid-loaded conditions. To properly assess autophagic flux, we co-treated cells with bafilomycin A1 (BafA, 20 nM) to block autophagosome-lysosome fusion [53], allowing us to distinguish between autophagosome accumulation and active flux enhancement, especially because static changes in LC3 may reflect either enhanced autophagosome biogenesis or a block in later steps of the pathway [54,55]. Under basal conditions, BafA co-treatment elevated both LC3-II/I ratio (Fig. 4F,G) and LC3 puncta in GLA-treated cells (Fig. 4H,I), reflecting active baseline autophagic turnover. However, BafA failed to increase LC3 puncta in the OP group supporting the conclusion that steatotic cells exhibit impaired autophagic flux in the absence of BafA, as already reported in other studies [56–58]. Remarkably, GLA treatment restored this functional flux, causing a significant increase in LC3 puncta in BafA-treated cells (Fig. 4H,I).

Then, to evaluate the physical association between LDs and lysosomes, we quantified LDs-LAMP1 colocalization (Fig. 5A-C, Suppl. Fig. 5A,B). Under basal conditions, GLA treatment markedly increased the signal overlap between LDs and LAMP1 (quantified by Manders' overlap coefficients tM1 and tM2, Fig. 5B,C). Importantly, AMPK inhibition with Compound C (CC) completely abolished GLA induced LDs-LAMP1 overlap, demonstrating that GLA activates the lipophagy pathway in an AMPK-dependent manner (Fig. 5A-C). In steatotic cells, despite the activation of the autophagic flux (Fig. 4F,G), LDs-LAMP1 overlap (tM1) remained unchanged, whereas tM2 (LAMP1-LDs overlap) increased (Fig. 5A-C). Nevertheless, a functional correlation between this enhanced autophagic capability and lipid breakdown is supported by AMPK inhibition. Indeed, pharmacological inhibition of AMPK using CC blocked the clearance of the LDs (Fig. 5D-F), leading to a high number of LDs (Fig. 5E) with reduced volume (Fig. 5F). This could be explained by the uncoupling of lipolysis, driven by PKA and still active in the presence of CC, and lipophagy, which cannot eliminate these small droplets when AMPK is inhibited, leading to their accumulation. This finding aligns with established models showing that suppression of AMPK signaling prevents the mobilization of LDs toward autophagic degradation, thereby blocking lipophagy [59].

Collectively, our results show that GLA activates lipophagy under basal conditions and restores the autophagic flux in steatotic ones, suggesting that the AMPK-mediated enhanced autophagic capacity is a key mechanism for lipid clearance under conditions of lipid overload.

Glabranin restores mitochondrial bioenergetics and oxidative flux in steatotic conditions

The free fatty acids released through lipolysis and lipophagy are generally funneled into mitochondrial oxidation to prevent lipotoxicity [60] (Fig. 6A). In line with this, quantitative proteomics showed that GLA treatment upregulates enzymes involved in lipid catabolism, fatty-acid β-oxidation, TCA cycle flux, and selective autophagy (Supplementary Table 1; Fig. 2A), indicating a coordinated activation of oxidative metabolism. In line with this signature, GLA enhanced mitochondrial membrane potential without altering mitochondrial mass, as reflected by the increased $DiOC_6$/MitoTracker ratio (Fig. 6B).

To better evaluate the functional effect of GLA on mitochondrial activity, we performed real-time bioenergetic profiling with the Seahorse system. As expected, steatotic cells exhibited a marked reduction in oxygen consumption rate (OCR) (Fig. 6C), consistent with previous observations [61]. GLA treatment restored oxygen consumption rate across all phases of the Mito Stress Test, normalizing respiratory performance to non-steatotic levels. Quantitative analysis confirmed significant increases in basal and maximal respiration, spare respiratory capacity, and ATP-linked oxygen consumption (Fig. 6D).

Functional fatty acid oxidation (FAO) assays corroborated this metabolic mechanism: GLA markedly increased the fluorescence generated by cleavage of the coumarin-based palmitate analogue FAO Blue (Fig. 6E-F), indicating accelerated mitochondrial β-oxidation of long-chain fatty acids. Consistently, in a Seahorse FAO assay, GLA significantly enhanced mitochondrial oxygen consumption in cells exposed to palmitate (Fig. 6G), supporting a robust stimulation of FAO-driven respiration.

Together, these findings suggest that GLA stimulates mitochondrial function by increasing mitochondrial polarization, respiratory reserve, and oxidative capacity, thereby enabling steatotic cells to efficiently channel excess lipids, mobilized via lipophagy and lipolysis, into β-oxidation.

Glabranin treatment reverses the negative effects of a high-fat diet in *Drosophila melanogaster*

To investigate the effect of GLA in a multicellular model, we orally administered GLA to *Drosophila melanogaster* male flies fed a high-fat diet (FD, Fig. 7A), a well-established model displaying features that closely resemble mammalian metabolic syndrome [62]. After four days, fat bodies were dissected and stained with Nile Red to visualize LDs. Morphological analysis of adipose tissue revealed that, as expected, the FD increased the number of LDs in the fat bodies of the flies. Remarkably, GLA supplementation induced significant remodeling of LDs morphology, with a reduction in the number of LDs per cell and an increase in LDs volumes (Fig. 7B-D). These

observations suggest that GLA profoundly modifies LDs organization *in vivo* under high-fat diet conditions.

Consistent with previous reports showing that a high-fat diet compromises fly locomotor performance [63,64], the climbing assay revealed a pronounced impairment in climbing ability after 3 days of exposure to FD (Fig. 7E). Interestingly, GLA supplementation significantly improved climbing performance, with FD+GLA flies displaying significantly higher AUC (area under the curve) values than FD flies (Tukey's multiple-comparison test, p=0.0321). Notably, climbing performance in FD+GLA flies was restored to a level comparable to those of CNT and GLA flies (adjusted p=0.09906 and p=0.9778, respectively) (Fig. 7E). To determine whether these functional improvements translated into enhanced organismal resilience, survival was monitored for two weeks in flies maintained on the high-fat diet with or without GLA supplementation. Kaplan-Meier analysis revealed significantly improved survival in the FD+GLA group compared with FD-fed flies (log-rank test, $\chi^2 = 5.39$, $p = 0.0203$). The restricted mean survival time was 10.37 days (95% CI, 8.89-11.85) in FD+GLA flies compared with 8.78 days (95% CI, 7.32-10.24) in FD-fed flies (Fig. 7F). These findings indicate that GLA supplementation enhances survival under high-fat diet conditions (Fig. 7F), supporting its beneficial effects on organismal fitness under metabolic stress.

Discussion

MAFLD is recognized as the most prevalent chronic liver disorder worldwide, affecting an estimated 25-30% of the global population, with higher incidence in individuals with obesity, type 2 diabetes, dyslipidemia, and metabolic syndrome [65]. Its rising burden reflects the global increase in sedentary lifestyle, caloric excess, and insulin resistance. Prevention relies primarily on lifestyle interventions, including sustained weight reduction, regular physical activity, improved dietary quality, and control of cardiometabolic risk factors.

Natural bioactive molecules can exert significant regulatory effects on lipid dysmetabolism by targeting key metabolic nodes involved in cholesterol handling, fatty-acid oxidation, and lipogenesis [23,66]. Among the most effective compounds,

berberine enhances LDL clearance and improves hepatic lipid flux through activation of AMPK and suppression of PCSK9, while monacolin K acts as a natural HMG-CoA reductase inhibitor, producing statin-like reductions in LDL cholesterol [67,68]. In addition, EGCG and resveratrol promote fatty-acid oxidation through AMPK and the SIRT1-PGC-1α axis [69–72]. Collectively, these molecules act through complementary mechanisms to improve lipid profiles, reduce hepatic steatosis, and manage the metabolic disturbances characteristic of dyslipidemia and metabolic syndrome.

In this paper, we demonstrate that glabranin is a novel bioactive compound capable of counteracting lipid dysmetabolism by reprogramming hepatic lipid handling toward a predominantly catabolic state and enhancing fatty acid oxidation. Glabranin belongs to the chemical class of prenylated flavonoids, which have gained significant interest for their potent metabolic and insulin-sensitizing activities [73]. Recently, glabranin has been described as a novel NRF2 activator, showing antioxidant effects in neuroblastoma cells [74]. Oxidative stress plays a major role in several pathologies, including MAFLD. Indeed, we show that activation of the NRF2-dependent cellular response is able to reduce lipid peroxidation, positioning glabranin within the growing class of prenylated flavonoids with therapeutic potential for MAFLD and metabolic syndrome.

From a chemical and sourcing perspective, glabranin offers additional advantages that support its further investigation. Glabranin is the C8-prenylated derivative of pinocembrin, a flavanone extensively investigated for its broad pharmacological activities [75,76]. Prenylation is particularly relevant in flavonoids because it generally increases lipophilicity and membrane affinity and may favor tissue accumulation [77,78]. Thus, glabranin combines a well-characterized flavanone scaffold with the physicochemical properties conferred by C-prenylation. Importantly, glabranin can be selectively recovered from *G. glabra* leaves, an underutilized side-stream of the licorice supply chain, through a green supercritical CO_2 extraction process yielding a solvent-free flavanone-enriched extract containing approximately 6% (w/w) glabranin [25]. The compound can then be isolated at >95% purity through an automated purification procedure, providing a sustainable and potentially scalable route for its production.

Mechanistically, glabranin stimulates PKA activation through increased cAMP levels (Fig. 3B). cAMP signaling is a central regulator of lipid metabolism: insulin suppresses intracellular cAMP to inhibit lipolysis and promote triglyceride storage [79]. Multiple adenylate cyclase isoforms contribute to cAMP production across tissues, with ADCY5 acting as the predominant isoform controlling hepatic lipid metabolism. Most ADCYs are transmembrane enzymes, whereas ADCY10 represents the soluble variant. These isoforms exhibit distinct regulatory properties and are differentially modulated by G proteins, Ca^{2+}, and various post-translational modifications. In addition, several pharmacological activators and inhibitors of these enzymes have been identified [79]. Concurrently, phosphodiesterases serve as key regulators of cAMP degradation, further increasing the complexity of intracellular cAMP signaling dynamics. Even without identifying the precise isoform involved, our data clearly demonstrate that glabranin activates the cAMP-PKA-LKB1-AMPK axis (Fig. 3-4), resulting in a measurable increase in downstream cAMP-dependent signaling. Activation of the PKA pathway has been previously shown to stimulate hepatocellular lipolysis [47], promoting a robust catabolic breakdown of LDs. Here, we further demonstrate that glabranin-induced PKA activation enhances AMPK signaling through a phosphorylation-dependent modulation of LKB1 (Fig. 4A-C), thereby amplifying a metabolic program that favors the lipophagic clearance of smaller LDs. Remarkably, glabranin treatment does not affect the mTORC1 pathway, the other major regulator of autophagy (Suppl. Fig. S6A), reinforcing the conclusion that AMPK, rather than mTORC1, is the principal driver of GLA-induced autophagy. Strikingly, simultaneous pharmacological inhibition of PKA and AMPK produced the same effect as AMPK inhibition alone, supporting a linear PKA-AMPK axis in LDs catabolism (Suppl. Fig. S6B-C), in which lipolysis and lipophagy operate as coordinated pathways: PKA-driven lipolysis initiates LDs size reduction, while AMPK-dependent lipophagy completes their degradation (Fig. 8). This sequential processing prevents an acute cytosolic accumulation of free fatty acids, thereby avoiding lipotoxicity and preserving mitochondrial integrity [47,80].

Interestingly, the structurally related compound glabridin, a well-known prenylated isoflavonoid from licorice roots, has been reported to attenuate lipid accumulation through coordinated activation of the AMPK and MAPK pathways [81]. Notably, however, glabridin requires relatively high concentrations (up to 8 mM), to elicit

measurable metabolic effects [81] (Suppl. Fig. S7A-C). In sharp contrast, our data show that glabranin is nontoxic and markedly reduces LD accumulation at only 9.2 µM, a concentration approximately one thousand-fold lower. Moreover, glabranin is rapidly internalized within 10 minutes (Fig. 1F), underscoring its potential as a highly promising candidate for therapeutic development at lower and safer pharmacological doses.

The metabolic fate of the fatty acids released by the dual PKA-AMPK program is a decisive determinant in reversing hepatic steatosis. Our data, supported by proteomic profiling, indicate that glabranin does not merely mobilize lipids, which cause lipotoxicity, oxidative stress, and mitochondrial dysfunction, but efficiently drives their catabolic disposal through mitochondrial β-oxidation (Fig. 6, 8). Glabranin robustly restored oxygen-consumption rates, which are typically suppressed under steatotic conditions, and markedly increased palmitate flux into the oxidative machinery, demonstrating a coherent enhancement of mitochondrial fatty acid clearance.

Although our findings delineate a previously unrecognized mechanism of action for glabranin, the evidence presented here likely captures only a fraction of its functional landscape. Additional studies will be required to define how glabranin governs LDs biogenesis in the ER, as well as the turnover and cycling of LD-associated proteins. Dissecting this spatial redistribution and its feedback on ER homeostasis will be essential to clarify the extent to which glabranin reshapes hepatocellular metabolic programs, in line with the emerging paradigm of modulating LD dynamics through natural compounds.

Remarkably, glabranin treatment not only induced a marked remodeling of LD organization but also significantly improved locomotor performance in the obese *Drosophila melanogaster* model (Fig. 7), in which diet-induced steatosis is known to impair neuromuscular function and shorten lifespan [82]. Consistent with these observations, glabranin improves survival under high-fat diet conditions, highlighting its ability to counteract the detrimental effects of metabolic stress at the organismal level.

Conclusions

Collectively, our findings indicate that glabranin acts as a metabolic orchestrator: it initiates the breakdown of neutral lipid stores and subsequently ensures their complete disposal by enhancing mitochondrial oxidative efficiency. The coordinated linkage between lipid mobilization and final catabolic disposal constitutes a key protective mechanism against lipotoxicity and a driver of hepatic homeostasis, laying a robust groundwork for future investigations into its translational potential in advanced steatosis models.

List of abbreviations

AMPK AMP-activated protein kinase
cAMP cyclic AMP
ER endoplasmic reticulum
FAO fatty acid oxidation
FFA free fatty acids
LD lipid droplet
LKB1 Liver Kinase B1
MAFLD Metabolic dysfunction-associated fatty liver disease
NAFLD non-alcoholic fatty liver disease
NASH non-alcoholic steatohepatitis
NRF2 Nuclear factor erythroid 2-related factor 2
OCR oxygen consumption rate
PKA protein kinase A
PLIN2 Perilipin 2

Declarations

Ethics approval and consent to participate. Not applicable.

Consent for publication. Not applicable.

Availability of data and materials. The mass spectrometry proteomics data have been deposited to the ProteomeXchange Consortium via the PRIDE (Vizcaíno et al., 2016) partner repository, with the dataset identifier PXD083442. All other data will be made available from the corresponding author upon request.

Competing interests. The authors declare that they have no known competing financial interests or personal relationships that could have appeared to influence the work reported in this paper.

Funding. Project funded under the National Recovery and Resilience Plan (NRRP), Mission 4. Component 2 Investment 1.4—Call for tender No. 3138 of December 16, 2021, rectified by Decree n.3175 of December 18, 2021 of Italian Ministry of University and Research funded by the European Union—NextGenerationEU; Award Number: Project code CN_00000033, Concession Decree No. 1034 of June 17, 2022. Adopted by the Italian Ministry of University and Research, CUP, H43C22000530001, Spoke 6, Project title “National Biodiversity Future Center—NBFC”. Project funded under the National Recovery and Resilience Plan (NRRP), Mission 4. Component 2 Investment 1.3—Call for tender No. 3138, 16 December 2021, rectified by Decree n.341 of 15 March 2022 of Italian Ministry of University and Research funded by the European Union—NextGenerationEU; Project code PE0000003 ON FOODS—CUP:H43C22000820001—Spoke 6, Project title “ON Foods—Research and innovation network on food and nutrition Sustainability, Safety and Security—Working ON Foods”. Project *“Bio-waste products as a source of nutraceuticals to target the common trait of inflammation in cancer and neurodegeneration”* Prot. 2022LW54KC, Bando PRIN 2022 - D.D. n. 104 of 02/02/202, Mission 4. Component 2 from Research to Industry, Investment 1.1, funded by the European Union—NextGenerationEU.

Authors' contributions.

H.M.: Investigation; Visualization; Writing – original draft; Writing – review & editing.

G.S.: Investigation; Visualization; Writing – review & editing.

D.B.: Investigation; Writing – original draft; Writing – review & editing; Funding acquisition.

V.S.: Investigation.

S.S.: Investigation.

A:L.P.: Supervision; Writing – review & editing; Conceptualization.

E:M.: Investigation; Visualization; Writing – review & editing.

G.T.: Investigation; Visualization; Supervision; Writing – original draft.

M.L.: Project administration; Funding acquisition.

B.S.: Supervision; Writing – review & editing.

F.T.: Investigation; Validation; Visualization; Supervision; Writing – original draft; Writing – review & editing.

P.C.: Writing – original draft; Writing – review & editing; Conceptualization; Supervision; Project administration; Funding acquisition.

Acknowledgements

We acknowledge Dirk Pijnenburg (PAMGENE) for kinome analysis and Maura Brioschi for the glabranin internalization analysis.

We thank David U. Mick Lab (Medical Biochemistry and Molecular Biology, Center for Molecular Signaling (PZMS), Faculty of Medicine, Saarland University, Germany) for providing the anti-pS428-LKB1 and anti-LKB1 antibodies.

References

1. Targher G, Valenti L, Byrne CD. Metabolic Dysfunction-Associated Steatotic Liver Disease. N Engl J Med. 2025;393:683–98. https://doi.org/10.1056/NEJMra2412865

2. Younossi Z, Tacke F, Arrese M, Chander Sharma B, Mostafa I, Bugianesi E, et al. Global Perspectives on Nonalcoholic Fatty Liver Disease and Nonalcoholic Steatohepatitis. Hepatology. Baltimore, Md.; 2019;69:2672–82. https://doi.org/10.1002/hep.30251

3. Chalasani N, Younossi Z, Lavine JE, Charlton M, Cusi K, Rinella M, et al. The diagnosis and management of nonalcoholic fatty liver disease: Practice guidance from

the American Association for the Study of Liver Diseases. Hepatology. Baltimore, Md.; 2018;67:328–57. https://doi.org/10.1002/hep.29367

4. Hallsworth K, Adams LA. Lifestyle modification in NAFLD/NASH: Facts and figures. JHEP Rep Innov Hepatol. 2019;1:468–79. https://doi.org/10.1016/j.jhepr.2019.10.008

5. Schulze RJ, McNiven MA. Lipid Droplet Formation and Lipophagy in Fatty Liver Disease. Semin Liver Dis. 2019;39:283–90. https://doi.org/10.1055/s-0039-1685524

6. Gu X, Luo Y, Zhang J, Ouyang H, Kong Z, Wang T, et al. The therapeutic role of natural compounds mediated through Nrf2 in metabolic dysfunction-associated steatotic liver disease. Biochem Pharmacol. 2026;250:117989. https://doi.org/10.1016/j.bcp.2026.117989

7. Arroyave-Ospina JC, Wu Z, Geng Y, Moshage H. Role of Oxidative Stress in the Pathogenesis of Non-Alcoholic Fatty Liver Disease: Implications for Prevention and Therapy. Antioxidants. Basel, Switzerland; 2021;10:174. https://doi.org/10.3390/antiox10020174

8. Wang Y-L, Wu J, Li R-X, Sun Y-T, Ma Y-J, Zhao C-Y, et al. A double-edged sword: The Kelch-like ECH-associated protein 1-nuclear factor erythroid-derived 2-related factor 2-antioxidant response element pathway targeted pharmacological modulation in nonalcoholic fatty liver disease. Curr Opin Pharmacol. 2021;60:281–90. https://doi.org/10.1016/j.coph.2021.07.021

9. Liu K, Czaja MJ. Regulation of lipid stores and metabolism by lipophagy. Cell Death Differ. 2013;20:3–11. https://doi.org/10.1038/cdd.2012.63

10. Kloska A, Węsierska M, Malinowska M, Gabig-Cimińska M, Jakóbkiewicz-Banecka J. Lipophagy and Lipolysis Status in Lipid Storage and Lipid Metabolism Diseases. Int J Mol Sci. 2020;21:6113. https://doi.org/10.3390/ijms21176113

11. Lipke K, Kubis-Kubiak A, Piwowar A. Molecular Mechanism of Lipotoxicity as an Interesting Aspect in the Development of Pathological States-Current View of Knowledge. Cells. 2022;11:844. https://doi.org/10.3390/cells11050844

12. Qiu S, Liang Z, Wu Q, Wang M, Yang M, Chen C, et al. Hepatic lipid accumulation induced by a high-fat diet is regulated by Nrf2 through multiple pathways. FASEB J Off Publ Fed Am Soc Exp Biol. 2022;36:e22280. https://doi.org/10.1096/fj.202101456R

13. Han Y, Hu Z, Cui A, Liu Z, Ma F, Xue Y, et al. Post-translational regulation of lipogenesis via AMPK-dependent phosphorylation of insulin-induced gene. Nat Commun. 2019;10:623. https://doi.org/10.1038/s41467-019-08585-4

14. Hardie DG, Pan DA. Regulation of fatty acid synthesis and oxidation by the AMP-activated protein kinase. Biochem Soc Trans. 2002;30:1064–70. https://doi.org/10.1042/bst0301064

15. Foretz M, Viollet B. Activation of AMPK for a Break in Hepatic Lipid Accumulation and Circulating Cholesterol. EBioMedicine. 2018;31:15–6. https://doi.org/10.1016/j.ebiom.2018.05.009

16. Sepúlveda-Fragoso V, Barreto-Reis E, Carvalho-Laureano T de S, Stockler-Pinto MB, Frantz EDC, de Carvalho DP, et al. Bisphenol S induces hepatic steatosis and insulin resistance through AMPK inhibition and endoplasmic reticulum stress. Food Chem Toxicol Int J Publ Br Ind Biol Res Assoc. 2026;215:116222. https://doi.org/10.1016/j.fct.2026.116222

17. Svegliati-Baroni G, Pierantonelli I, Torquato P, Marinelli R, Ferreri C, Chatgilialoglu C, et al. Lipidomic biomarkers and mechanisms of lipotoxicity in non-alcoholic fatty liver disease. Free Radic Biol Med. 2019;144:293–309. https://doi.org/10.1016/j.freeradbiomed.2019.05.029

18. Sanyal AJ, Chalasani N, Kowdley KV, McCullough A, Diehl AM, Bass NM, et al. Pioglitazone, Vitamin E, or Placebo for Nonalcoholic Steatohepatitis. N Engl J Med. Massachusetts Medical Society; 2010;362:1675–85. https://doi.org/10.1056/NEJMoa0907929

19. Armstrong MJ, Gaunt P, Aithal GP, Barton D, Hull D, Parker R, et al. Liraglutide safety and efficacy in patients with non-alcoholic steatohepatitis (LEAN): a multicentre, double-blind, randomised, placebo-controlled phase 2 study. Lancet. London, England; 2016;387:679–90. https://doi.org/10.1016/S0140-6736(15)00803-X

20. Fang X, Song J, Zhou K, Zi X, Sun B, Bao H, et al. Molecular Mechanism Pathways of Natural Compounds for the Treatment of Non-Alcoholic Fatty Liver Disease. Molecules. Basel, Switzerland; 2023;28:5645. https://doi.org/10.3390/molecules28155645

21. Moukham H, Lambiase A, Barone GD, Tripodi F, Coccetti P. Exploiting Natural Niches with Neuroprotective Properties: A Comprehensive Review. Nutrients. 2024;16:1298. https://doi.org/10.3390/nu16091298

22. Omidkhoda N, Mahdiani S, Hayes AW, Karimi G. Natural compounds against nonalcoholic fatty liver disease: A review on the involvement of the LKB1/AMPK signaling pathway. Phytother Res PTR. 2023;37:5769–86. https://doi.org/10.1002/ptr.8020

23. Zhang C, Shi J, Shi L. Natural products intervene in non-alcoholic fatty liver disease by regulating the AMPK signaling pathway: preclinical evidence and mechanism. Front Pharmacol [Internet]. Frontiers; 2025 [cited 2026 Sep 7];16. https://doi.org/10.3389/fphar.2025.1696506

24. Docimo T, Celano R, Lambiase A, Di Sanzo R, Serio S, Santoro V, et al. Exploring Influence of Production Area and Harvest Time on Specialized Metabolite Content of Glycyrrhiza glabra Leaves and Evaluation of Antioxidant and Anti-Aging Properties. Antioxidants. Basel, Switzerland; 2024;13:93. https://doi.org/10.3390/antiox13010093

25. Serio S, Lambiase A, Santoro V, Piccinelli AL, Celano R, Spandri G, et al. Selective Recovery of Flavanone-Enriched Fractions from Glycyrrhiza Glabra Leaves by Supercritical CO2 Extraction with Neuroprotective Potential. Antioxidants. Basel, Switzerland; 2026;15:874. https://doi.org/10.3390/antiox15070874

26. Celano R, Docimo T, Piccinelli AL, Rizzo S, Campone L, Di Sanzo R, et al. Specialized metabolite profiling of different *Glycyrrhiza glabra* organs by untargeted UHPLC-HRMS. Ind Crops Prod. 2021;170:113688. https://doi.org/10.1016/j.indcrop.2021.113688

27. Xie Z, Bailey A, Kuleshov MV, Clarke DJB, Evangelista JE, Jenkins SL, et al. Gene Set Knowledge Discovery with Enrichr. Curr Protoc. 2021;1:e90. https://doi.org/10.1002/cpz1.90

28. Negri A, Tedeschi G, Ceciliani F, Ronchi S. Purification of beef kidney d-aspartate oxidase overexpressed in *Escherichia coli* and characterization of its redox potentials and oxidative activity towards agonists and antagonists of excitatory amino acid receptors. Biochim Biophys Acta BBA - Protein Struct Mol Enzymol. 1999;1431:212–22. https://doi.org/10.1016/S0167-4838(99)00027-8

29. Vernocchi V, Morselli MG, Varesi S, Nonnis S, Maffioli E, Negri A, et al. Sperm ubiquitination in epididymal feline semen. Theriogenology. 2014;82:636–42. https://doi.org/10.1016/j.theriogenology.2014.06.002

30. Schulte C, Ripamonti M, Maffioli E, Cappelluti MA, Nonnis S, Puricelli L, et al. Scale Invariant Disordered Nanotopography Promotes Hippocampal Neuron Development and Maturation with Involvement of Mechanotransductive Pathways. Front Cell Neurosci [Internet]. Frontiers; 2016 [cited 2026 Sep 4];10. https://doi.org/10.3389/fncel.2016.00267

31. Mi H, Muruganujan A, Huang X, Ebert D, Mills C, Guo X, et al. Protocol Update for large-scale genome and gene function analysis with the PANTHER classification system (v.14.0). Nat Protoc. 2019;14:703–21. https://doi.org/10.1038/s41596-019-0128-8

32. Szklarczyk D, Kirsch R, Koutrouli M, Nastou K, Mehryary F, Hachilif R, et al. The STRING database in 2023: protein-protein association networks and functional enrichment analyses for any sequenced genome of interest. Nucleic Acids Res. 2023;51:D638–46. https://doi.org/10.1093/nar/gkac1000

33. Madabattula ST, Strautman JC, Bysice AM, O'Sullivan JA, Androschuk A, Rosenfelt C, et al. Quantitative Analysis of Climbing Defects in a Drosophila Model of Neurodegenerative Disorders. J Vis Exp JoVE. 2015;e52741. https://doi.org/10.3791/52741

34. Ott RK, Williams IH, Armstrong AR. Improved whole-mount immunofluorescence protocol for consistent and robust labeling of adult Drosophila melanogaster adipose tissue. Biol Open. 2024;13:bio060491. https://doi.org/10.1242/bio.060491

35. Gómez-Lechón MJ, Donato MT, Martínez-Romero A, Jiménez N, Castell JV, O'Connor J-E. A human hepatocellular *in vitro* model to investigate steatosis. Chem Biol Interact. 2007;165:106–16. https://doi.org/10.1016/j.cbi.2006.11.004

36. Nguyen TB, Louie SM, Daniele JR, Tran Q, Dillin A, Zoncu R, et al. DGAT1-Dependent Lipid Droplet Biogenesis Protects Mitochondrial Function during

Starvation-Induced Autophagy. Dev Cell. 2017;42:9-21.e5. https://doi.org/10.1016/j.devcel.2017.06.003

37. Faulkner CS, White CM, Shah VH, Jophlin LL. A single nucleotide polymorphism of *PLIN2* is associated with nonalcoholic steatohepatitis and causes phenotypic changes in hepatocyte lipid droplets: A pilot study. Biochim Biophys Acta BBA - Mol Cell Biol Lipids. 2020;1865:158637. https://doi.org/10.1016/j.bbalip.2020.158637

38. Bailey AP, Koster G, Guillermier C, Hirst EMA, MacRae JI, Lechene CP, et al. Antioxidant Role for Lipid Droplets in a Stem Cell Niche of *Drosophila*. Cell. 2015;163:340–53. https://doi.org/10.1016/j.cell.2015.09.020

39. Chen W, Xue D, Feng X, Zhong Y, Li Q, Zhang W, et al. Pinocembrin ameliorates non-alcoholic fatty liver disease by activating Nrf2/HO-1 and inhibiting the NF-κB signaling pathway. Histol Histopathol. 2025;40:1817–28. https://doi.org/10.14670/HH-18-893

40. Zhang Z, He Z, Wang X, Huang B, Zhang W, Sha Y, et al. A natural small molecule pinocembrin resists high-fat diet-induced obesity through GPR120-ERK1/2 pathway. J Nutr Biochem. 2025;135:109772. https://doi.org/10.1016/j.jnutbio.2024.109772

41. Simons R, Gruppen H, Bovee TFH, Verbruggen MA, Vincken J-P. Prenylated isoflavonoids from plants as selective estrogen receptor modulators (phytoSERMs). Food Funct. 2012;3:810–27. https://doi.org/10.1039/c2fo10290k

42. Frattaruolo L, Lauria G, Aiello F, Carullo G, Curcio R, Fiorillo M, et al. Exploiting Glycyrrhiza glabra L. (Licorice) Flavanones: Licoflavanone's Impact on Breast Cancer Cell Bioenergetics. Int J Mol Sci. Multidisciplinary Digital Publishing Institute; 2024;25:7907. https://doi.org/10.3390/ijms25147907

43. Frattaruolo L, Carullo G, Brindisi M, Mazzotta S, Bellissimo L, Rago V, et al. Antioxidant and Anti-Inflammatory Activities of Flavanones from Glycyrrhiza glabra L. (licorice) Leaf Phytocomplexes: Identification of Licoflavanone as a Modulator of NF-kB/MAPK Pathway. Antioxidants. Multidisciplinary Digital Publishing Institute; 2019;8:186. https://doi.org/10.3390/antiox8060186

44. Shin SM, Yang JH, Ki SH. Role of the Nrf2-ARE pathway in liver diseases. Oxid Med Cell Longev. 2013;2013:763257. https://doi.org/10.1155/2013/763257

45. Nakatsuji M, Shibano M, Fujimori K. Antioxidant Activity of Flavonoid Glabranin by Upregulating Antioxidant Gene Expression via MEK/ERK and PI3K/Akt Pathways in Human Neuroblastoma SH-SY5Y Cells. Neurochem Res. 2026;51:141. https://doi.org/10.1007/s11064-026-04759-x

46. Chitraju C, Mejhert N, Haas JT, Diaz-Ramirez LG, Grueter CA, Imbriglio JE, et al. Triglyceride Synthesis by DGAT1 Protects Adipocytes from Lipid-Induced ER Stress during Lipolysis. Cell Metab. 2017;26:407-418.e3. https://doi.org/10.1016/j.cmet.2017.07.012

47. Schott MB, Rasineni K, Weller SG, Schulze RJ, Sletten AC, Casey CA, et al. β-Adrenergic induction of lipolysis in hepatocytes is inhibited by ethanol exposure. J Biol Chem. 2017;292:11815–28. https://doi.org/10.1074/jbc.M117.777748

48. Chen C, Gao H, Tian Q, Cao J. cAMP–PKA/EPAC signaling pathways: crucial regulators of lipid homeostasis. Adipocyte. Taylor & Francis; 2026;15:2603605. https://doi.org/10.1080/21623945.2025.2603605

49. Su C-L, Sztalryd C, Contreras JA, Holm C, Kimmel AR, Londos C. Mutational analysis of the hormone-sensitive lipase translocation reaction in adipocytes. J Biol Chem. 2003;278:43615–9. https://doi.org/10.1074/jbc.M301809200

50. Sztalryd C, Brasaemle DL. The perilipin family of lipid droplet proteins: Gatekeepers of intracellular lipolysis. Biochim Biophys Acta Mol Cell Biol Lipids. 2017;1862:1221–32. https://doi.org/10.1016/j.bbalip.2017.07.009

51. Shu G, Sun H, Zhang T, Zhu A, Lei X, Wang C, et al. Theaflavine inhibits hepatic stellate cell activation by modulating the PKA/LKB1/AMPK/GSK3β cascade and subsequently enhancing Nrf2 signaling. Eur J Pharmacol. 2023;956:175964. https://doi.org/10.1016/j.ejphar.2023.175964

52. Kari S, Vasko VV, Priya S, Kirschner LS. PKA Activates AMPK Through LKB1 Signaling in Follicular Thyroid Cancer. Front Endocrinol [Internet]. Frontiers; 2019 [cited 2026 Sep 4];10. https://doi.org/10.3389/fendo.2019.00769

53. Mauvezin C, Neufeld TP. Bafilomycin A1 disrupts autophagic flux by inhibiting both V-ATPase-dependent acidification and Ca-P60A/SERCA-dependent autophagosome-lysosome fusion. Autophagy. 2015;11:1437–8. https://doi.org/10.1080/15548627.2015.1066957

54. Klionsky DJ, Abdel-Aziz AK, Abdelfatah S, Abdellatif M, Abdoli A, Abel S, et al. Guidelines for the use and interpretation of assays for monitoring autophagy (4th edition)1. Autophagy. 2021;17:1–382. https://doi.org/10.1080/15548627.2020.1797280

55. Yoshii SR, Mizushima N. Monitoring and Measuring Autophagy. Int J Mol Sci. 2017;18:1865. https://doi.org/10.3390/ijms18091865

56. Chen X, Chan H, Zhang L, Liu X, Ho IHT, Zhang X, et al. The phytochemical polydatin ameliorates non-alcoholic steatohepatitis by restoring lysosomal function and autophagic flux. J Cell Mol Med. 2019;23:4290–300. https://doi.org/10.1111/jcmm.14320

57. Kim YJ, Lee JR, Kim MR, Jeong JA, Kim JJ, Jeong KW. Protein kinase-mediated inhibition of autophagy by palmitic acid in hepatocytes. Eur J Pharmacol. 2025;998:177528. https://doi.org/10.1016/j.ejphar.2025.177528

58. Mushtaq A, Ashraf NU, Altaf M. The mTORC1–G9a–H3K9me2 axis negatively regulates autophagy in fatty acid–induced hepatocellular lipotoxicity. J Biol Chem. 2023;299:102937. https://doi.org/10.1016/j.jbc.2023.102937

59. Kim J, Kundu M, Viollet B, Guan K-L. AMPK and mTOR regulate autophagy through direct phosphorylation of Ulk1. Nat Cell Biol. 2011;13:132–41. https://doi.org/10.1038/ncb2152

60. Hwang JS, Lai TH, Kim DR. Targeting Lipophagy in Liver Diseases: Impact on Oxidative Stress and Steatohepatitis. Antioxidants. 2025;14:908. https://doi.org/10.3390/antiox14080908

61. Guo B, Zhou Y, Liu B, He Y, Chen F, Cheng K-W. Lipid-Lowering Bioactivity of Microalga Nitzschia laevis Extract Containing Fucoxanthin in Murine Model and Carcinomic Hepatocytes. Pharmaceuticals. Multidisciplinary Digital Publishing Institute; 2021;14:1004. https://doi.org/10.3390/ph14101004

62. Liao S, Amcoff M, Nässel DR. Impact of high-fat diet on lifespan, metabolism, fecundity and behavioral senescence in *Drosophila*. Insect Biochem Mol Biol. 2021;133:103495. https://doi.org/10.1016/j.ibmb.2020.103495

63. Jung J, Kim D-I, Han G-Y, Kwon HW. The Effects of High Fat Diet-Induced Stress on Olfactory Sensitivity, Behaviors, and Transcriptional Profiling in Drosophila melanogaster. Int J Mol Sci. Multidisciplinary Digital Publishing Institute; 2018;19:2855. https://doi.org/10.3390/ijms19102855

64. Rivera O, McHan L, Konadu B, Patel S, Sint Jago S, Talbert ME. A high-fat diet impacts memory and gene expression of the head in mated female Drosophila melanogaster. J Comp Physiol B. 2019;189:179–98. https://doi.org/10.1007/s00360-019-01209-9

65. Vancells Lujan P, Viñas Esmel E, Sacanella Meseguer E. Overview of Non-Alcoholic Fatty Liver Disease (NAFLD) and the Role of Sugary Food Consumption and Other Dietary Components in Its Development. Nutrients. Multidisciplinary Digital Publishing Institute; 2021;13:1442. https://doi.org/10.3390/nu13051442

66. Hu W, Gu M, Li H, Li H, Kan J, Zhang L, et al. Emerging natural products against obesity and metabolic dysfunction-associated steatotic liver disease/metabolic dysfunction-associated steatohepatitis: Direct target discovery and mechanistic insights. Pharmacol Rev. 2026;78:100125. https://doi.org/10.1016/j.pharmr.2026.100125

67. Cicero AFG, Fogacci F, Zambon A. Red Yeast Rice for Hypercholesterolemia: JACC Focus Seminar. J Am Coll Cardiol. 2021;77:620–8. https://doi.org/10.1016/j.jacc.2020.11.056

68. Hernandez AV, Hwang J, Nasreen I, Sicignano D, Pasupuleti V, Snow-Caroti K, et al. Impact of Berberine or Berberine Combination Products on Lipoprotein, Triglyceride and Biological Safety Marker Concentrations in Patients with Hyperlipidemia: A Systematic Review and Meta-Analysis. J Diet Suppl. 2024;21:242–59. https://doi.org/10.1080/19390211.2023.2212762

69. Baur JA, Sinclair DA. Therapeutic potential of resveratrol: the in vivo evidence. Nat Rev Drug Discov. 2006;5:493–506. https://doi.org/10.1038/nrd2060

70. Lagouge M, Argmann C, Gerhart-Hines Z, Meziane H, Lerin C, Daussin F, et al. Resveratrol improves mitochondrial function and protects against metabolic disease by activating SIRT1 and PGC-1alpha. Cell. 2006;127:1109–22. https://doi.org/10.1016/j.cell.2006.11.013

71. Zhang S, Xie H, Pan P, Wang Q, Yang B, Li Y, et al. EGCG alleviates heat-stress-induced fat deposition by targeting HSP70 through activation of AMPK-SIRT1-PGC-1α in porcine subcutaneous preadipocytes. Biochem Pharmacol. 2024;225:116250. https://doi.org/10.1016/j.bcp.2024.116250

72. Lee M-S, Lee S, Doo M, Kim Y. Green Tea (-)-Epigallotocatechin-3-Gallate Induces PGC-1α Gene Expression in HepG2 Cells and 3T3-L1 Adipocytes. Prev Nutr Food Sci. 2016;21:62–7. https://doi.org/10.3746/pnf.2016.21.1.62

73. Li D, Fan J, Du L, Ren G. Prenylated flavonoid fractions from Glycyrrhiza glabra alleviate insulin resistance in HepG2 cells by regulating the ERK/IRS-1 and PI3K/Akt signaling pathways. Arch Pharm Res. 2024;47:127–45. https://doi.org/10.1007/s12272-024-01485-2

74. Nakatsuji M, Shibano M, Fujimori K. Antioxidant Activity of Flavonoid Glabranin by Upregulating Antioxidant Gene Expression via MEK/ERK and PI3K/Akt Pathways in Human Neuroblastoma SH-SY5Y Cells. Neurochem Res. 2026;51:141. https://doi.org/10.1007/s11064-026-04759-x

75. Rasul A, Millimouno FM, Ali Eltayb W, Ali M, Li J, Li X. Pinocembrin: A Novel Natural Compound with Versatile Pharmacological and Biological Activities. BioMed Res Int. 2013;2013:379850. https://doi.org/10.1155/2013/379850

76. Elbatreek MH, Mahdi I, Ouchari W, Mahmoud MF, Sobeh M. Current advances on the therapeutic potential of pinocembrin: An updated review. Biomed Pharmacother. 2023;157:114032. https://doi.org/10.1016/j.biopha.2022.114032

77. Mukai R. Prenylation enhances the biological activity of dietary flavonoids by altering their bioavailability. Biosci Biotechnol Biochem. 2018;82:207–15. https://doi.org/10.1080/09168451.2017.1415750

78. Chang SK, Jiang Y, Yang B. An update of prenylated phenolics: Food sources, chemistry and health benefits. Trends Food Sci Technol. 2021;108:197–213. https://doi.org/10.1016/j.tifs.2020.12.022

79. Wu S, Chen Y, Zhang J, Zhang J. Adenylyl Cyclase (ADCY) Protein Family: Molecular Mechanisms and Therapeutic Potential in Glucose and Lipid Metabolism and Feeding Regulation. J Cell Physiol. John Wiley & Sons, Ltd; 2026;241:e70216. https://doi.org/10.1002/jcp.70216

80. Schulze RJ, Drižytė K, Casey CA, McNiven MA. Hepatic Lipophagy: New Insights into Autophagic Catabolism of Lipid Droplets in the Liver. Hepatol Commun. 2017;1:359–69. https://doi.org/10.1002/hep4.1056

81. Wang M, Zhang F, Zhou J, Gong K, Chen S, Zhu X, et al. Glabridin Ameliorates Alcohol-Caused Liver Damage by Reducing Oxidative Stress and Inflammation via

p38 MAPK/Nrf2/NF-κB Pathway. Nutrients. Multidisciplinary Digital Publishing Institute; 2023;15:2157. https://doi.org/10.3390/nu15092157

82. Gáliková M, Klepsatel P. Obesity and Aging in the Drosophila Model. Int J Mol Sci. 2018;19:1896. https://doi.org/10.3390/ijms19071896

Figure legends

Figure 1. Glabranin reduces lipid droplet (LD) accumulation in HepG2 cells

(A) Chemical structure of the molecules glabranin (GLA), licoflavonone (LICO), and pinocembrin (PINO).

(B) Representative fluorescence images of HepG2 cells stained with BODIPY 493/503 (LDs, green) and DAPI (nuclei, blue) after 24 h of co-treatment with glabranin (GLA), licoflavonone (LICO), and pinocembrin (PINO) in control (CNT) or OP conditions. Scale bars, 10 µm.

(C-D) Quantification of LD number (C) and volume (D, in fL) per cell after 24 h of treatment. Cells were treated with the compounds glabranin (GLA), licoflavonone (LICO), and pinocembrin (PINO) under the CNT or OP conditions. Significance was determined by unpaired Student's t-test (n=3).

(E) HepG2 cells were exposed for 24 h to increasing concentrations of glabranin. Cell viability was measured using an MTT assay. Data are presented as mean + standard deviation. Significance was determined by unpaired Student's t-test (n=3).

(F) Time course of intracellular/cell-associated level of GLA in HepG2 cells in steatotic condition, assayed by LC-MS analysis. Data are presented as mean + standard deviation and are expressed as pmol GLA/cell. Significance was determined by unpaired Student's t-test (n=6).

(G) Intracellular neutral lipid level measured by cytofluorimetric analysis in HepG2 cells after 24 h treatment. The graph compares the total neutral lipid level under both basal (CNT) and steatotic (OP) conditions, in the presence or absence of GLA. Data are presented as mean + standard deviation. Significance was determined by unpaired Student's t-test (n=2-4 for each group).

Figure 2. Glabranin enhances NRF2-mediated antioxidant defense

(A) Enrichment of differentially expressed proteins analysed in the comparisons GLA vs CNT, OP vs CNT and OP+GLA vs OP.

(B) Representative immunofluorescence images of HepG2 cells showing NRF2 localization. Cells were treated with a fatty acid mixture (OP) in the presence or

absence of 9.2 µM GLA. The panels show NRF2 antibody staining (green), DAPI (nuclei, blue), and the corresponding merged channels. Scale bars, 10 µm.

(C) Quantification of NRF2 nuclear concentration. Data represent the mean fluorescence intensity of NRF2 within the nuclear area after 24h of treatment under the indicated conditions (CNT, GLA, OP, and OP+GLA). Significance was determined by unpaired Student's t-test (n= 3).

(D) Representative Western blot analysis of total NRF2 expression in HepG2 cells following 24 h treatment with GLA under control or steatotic conditions. Vinculin was used as the loading control to ensure equal protein loading across samples.

(E) Densitometric quantification of total NRF2 protein levels. The graph shows the NRF2 expression levels normalized to vinculin as loading control. Data were obtained from HepG2 cells after 24 h of treatment under CNT or OP conditions, with or without GLA supplementation. Data are presented as mean + standard deviation. Significance was determined by unpaired Student's t-test (n=3).

(F) Cell viability assay under oxidative challenge. HepG2 cells were co-treated for 24 h with the indicated conditions (OP, OP+GLA) in the presence of increasing concentrations of hydrogen peroxide (H_2O_2, 0-100 µM). Cell viability was assessed to evaluate the immediate cytoprotective capacity of GLA. Significance was determined by unpaired Student's t-test (n=8-9).

(G) Relative lipid peroxidation levels. Cells were co-treated with OP and GLA for 24 h prior to the assay. Rates of lipid peroxidation were then assessed by incubating the cells with the BODIPY™ 581/591 C11 sensor for 30 minutes. Fluorescence was acquired in both red (non-oxidized) and green (oxidized) channels. Data represent the quantification of the oxidized fraction (green signal) obtained after total cell segmentation. Significance was determined by unpaired Student's t-test (n=3).

(H-I) Enrichments of the differentially active kinases of the comparison GLA vs CNT (H) and OP+GLA vs OP (I). Enrichment analysis was performed using EnrichR [27] on regulated kinases, according to the KEGG pathway database.

Figure 3. Glabranin activates the cAMP-PKA pathway to drive lipolysis and lipid droplet mobilization.

(A) Schematic representation of the cAMP-PKA signaling pathway governing lipid droplet mobilization. Activation of adenylate cyclase (AC) increases intracellular cAMP production, triggering downstream PKA activation. Activated PKA then phosphorylates Hormone-Sensitive Lipase (HSL) and facilitates the displacement or degradation of the LD-coating protein PLIN2, thereby driving lipid droplet mobilization and glycerol release.

(B) Intracellular cAMP levels. HepG2 cells were treated with GLA for 5 minutes. Control cells (CNT) were treated with an equal volume of EtOH as vehicle. Cells were

then lysed for the quantification of cAMP levels using a competitive ELISA assay. Data are normalized to the total protein content and expressed as pmol/µg prot. Significance was determined by unpaired Student's t-test. (n=8-10)

(C) Representative Western blot analysis of phosphorylated PKA substrates (pPKA substrates) in HepG2 cells. Control cells (CNT) were treated with an equal volume of EtOH as vehicle. Vinculin was used as the loading control to ensure equal protein loading.

(D) Densitometric quantification of pPKA substrates levels normalized to vinculin. Data are presented as mean + standard deviation. Significance was determined by unpaired Student's t-test (n=3).

(E) Representative fluorescence images of HepG2 cells stained with BODIPY 493/503 (LDs, green) and DAPI (nuclei, blue). Cells were co-treated for 24 h with OP, GLA, and the selective PKA inhibitor H89 (10 µM). Scale bars, 10 µm.

(F-G) Quantification of LD number (F) and volume (G, in fL) per cell, in the absence or presence of the PKA-inhibitor H89 (10 µM). Significance was determined by unpaired Student's t-test (n=3).

(H) Representative Western blot analysis of Hormone-Sensitive Lipase (HSL) phosphorylation at Ser563 and Ser660. Total HSL and vinculin were used as loading controls.

(I-J) Densitometric quantification of HSL phosphorylation at Ser563 (I) and Ser660 (J) relative to total HSL levels after 24 h treatment with GLA. Data are presented as mean + standard deviation. Significance was determined by unpaired Student's t-test (n=4).

(K) Representative Western blot of PLIN2 expression in HepG2 cells treated for 24 h under basal (CNT) and steatotic (OP) conditions, with or without GLA. Vinculin was used as loading control.

(L) Densitometric quantification of PLIN2 expression relative to vinculin. Data are presented as mean + standard deviation. Significance was determined by unpaired Student's t-test (n=3).

(M) Evaluation of glycerol release as a marker of lipolytic activity in HepG2 and Huh7 cells. Data are normalized to total protein content (nmol Gly/µg prot) after 24 h treatment of GLA. Data are presented as mean + standard deviation. Significance was determined by unpaired Student's t-test (n=3).

Figure 4. Glabranin regulates the AMPK pathway and stimulates the autophagic flux.

(A-B) Cells were treated for 24 h with GLA or EtOH as vehicle control. The blot shows the phosphorylation status of pS428-LKB1 (A), pS79-ACC1, pT172-AMPK (B) and their corresponding total levels. Vinculin was used as loading control.

(C-D-E) Quantification of Western analyses in A,B. Data are presented as mean + standard deviation. Significance was determined by unpaired Student's t-test (n=3).

(F) Western blot analysis of LC3-II/LC3-I levels in HepG2 cells after 6 h treatment, in the presence or absence of Bafilomycin A1 (BafA). HepG2 cells were treated for 6 h under the indicated conditions: CNT, OP, GLA, and OP+GLA. Vinculin is utilized as a loading control.

(G) Quantification of the LC3-II ratio. Data are presented as mean + standard deviation. Significance was determined by unpaired Student's t-test (n=3).

(H) Representative immunofluorescence images demonstrating autophagosome formation (LC3 puncta) in HepG2 cells. Cells were subjected to 6 h co-treatment under steatotic (OP) conditions, with or without glabranin (GLA), and in the presence or absence of 20 nM Bafilomycin A1 (BafA), to assess autophagic flux. Images display the autophagosome marker (LC3, red), lipid droplets (LDs, green), and DAPI (nuclei, blue). Merged images are shown. Scale bars, 10 μm.

(I) Quantification of the number of LC3 puncta per cell. The graph compares the number of LC3 puncta (representing formed autophagosomes) in the absence and presence of Bafilomycin A1 (BafA). Significance was determined by unpaired Student's t-test (n=2).

Figure 5. Glabranin enhances the lipophagic activity in an AMPK-dependent manner.

(A) Representative fluorescence images show the colocalization between LDs and the lysosomal marker LAMP1 in HepG2 cells. Cells were treated for 6 h under the indicated conditions (CNT, GLA, OP, OP+GLA). LDs were stained with LipidTOX (green) and LAMP1 was stained in red. Nuclei were counterstained with Hoechst (blue, not shown in the merge). Images represent a single focal plane (single Z-stack optical section) acquired on a confocal microscope. Arrows indicate colocalization between LAMP1 and LDs signals. Scale bars, 10 μm.

(B-C) Quantification of colocalization analysis performed across whole single cells between LDs and LAMP1 using Manders' coefficients tM1 (B) and tM2 (C) via Fiji/ImageJ software. Significance was determined by unpaired Student's t-test (n=3).

(D) Representative fluorescence images of HepG2 cells stained with BODIPY 493/503 (green) and DAPI (blue). Cells were co-treated for 24 h with OP, GLA, and the selective AMPK inhibitor Compound C (CC, 10 μM). Cells were fixed and stained with BODIPY 493/503 to visualize LDs and DAPI to mark nuclei. Scale bars, 10 μm.

(E-F) Average number (E) and volume (F, in fL) of LDs in HepG2 cells co-treated with the AMPK inhibitor CC. Significance was determined by unpaired Student's t-test (n = 3).

Figure 6. Glabranin enhances mitochondrial efficiency and β-oxidation in HepG2 cells.

(A) Schematic representation of the proposed catabolic mechanism. After stimulation of lipolysis and lipophagy, free fatty acids (FAs) are channeled into mitochondria to support organelle efficiency and fuel β-oxidation.

(B) GLA increases mitochondrial membrane potential. The bar graph shows the relative fluorescence intensity after 24 h treatment with GLA using Mitotracker green (estimating total mitochondrial mass), $DiOC_6$ (estimating membrane potential), and the $DiOC_6$/Mitotracker ratio (indicating functional mitochondrial efficiency). Significance was determined by unpaired Student's t-test (n=3-4).

(C) GLA increases the dynamic profile of the Oxygen Consumption Rate (OCR) measured by Seahorse XF Mitochondrial Stress Test. The graph shows the real-time changes in OCR across the experiment. The sequential injection of mitochondrial inhibitors Oligomycin (inhibitor of ATP synthase), FCCP (uncoupler), and Rotenone/Antimycin A (inhibitors of Complexes I and III) allows for the calculation of different respiratory parameters (presented in panel C). Data are presented as mean +/- standard error (n=4).

(D) Quantification of mitochondrial respiratory parameters derived from the Seahorse XF OCR profile. The box plot shows key parameters derived from the assay: basal respiration, maximal respiration, ATP production, and spare respiratory capacity. All data were normalized to CNT. Significance was determined by unpaired Student's t-test.

(E) Representative fluorescence images showing the uptake and metabolic processing of the fluorescent palmitate analog FAO Blue (blue signal). HepG2 cells were pre-treated for 24 h under steatotic conditions (OP) with or without GLA (control cells received EtOH as vehicle). Following pre-treatment, cells were incubated with the FAO sensor for 3 h prior to acquisition. Brightfield (BF) images are provided as morphological reference.

(F) Fluorescence intensity was extracted from segmented single cells to quantify the accumulation of the metabolized palmitate analog. Data are expressed as concentration intensity (a.u.). Significance was determined by unpaired Student's t-test. (n=3).

(G) Maximal respiration measured with FAO Seahorse analysis in cells pre-treated for 16 h with or without GLA (control cells received EtOH as vehicle) and supplied with

BSA (CNT) or palmitate (PALM). All data were normalized to CNT. Significance was determined by unpaired Student's t-test.

Figure 7. Glabranin treatment reverses the negative effects of a high fat diet in *Drosophila melanogaster*

(A) Schematic representation of the flies' treatments.

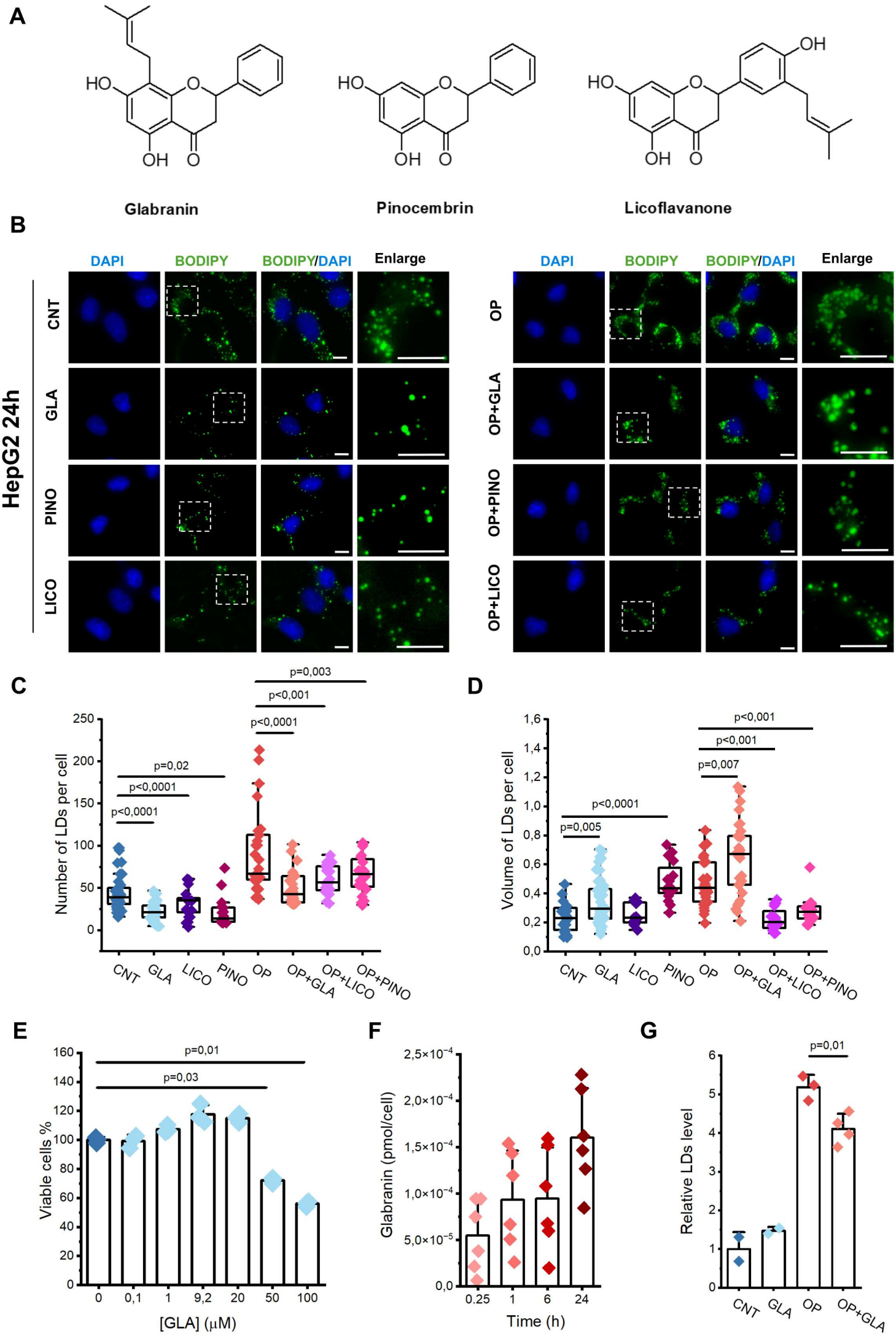
(B) Representative fluorescence microscopy images of flies' fat bodies. Fixed fat bodies of flies exposed to control (CNT) or fat diet (FD) for 4 days, with or without the supplementation of GLA. LDs were stained with Nile Red (red) and Alexa Fluor™ 488 phalloidin (green) to stain membranes, while nuclei were counterstained with DAPI (blue). Scale bars, 10 µm.

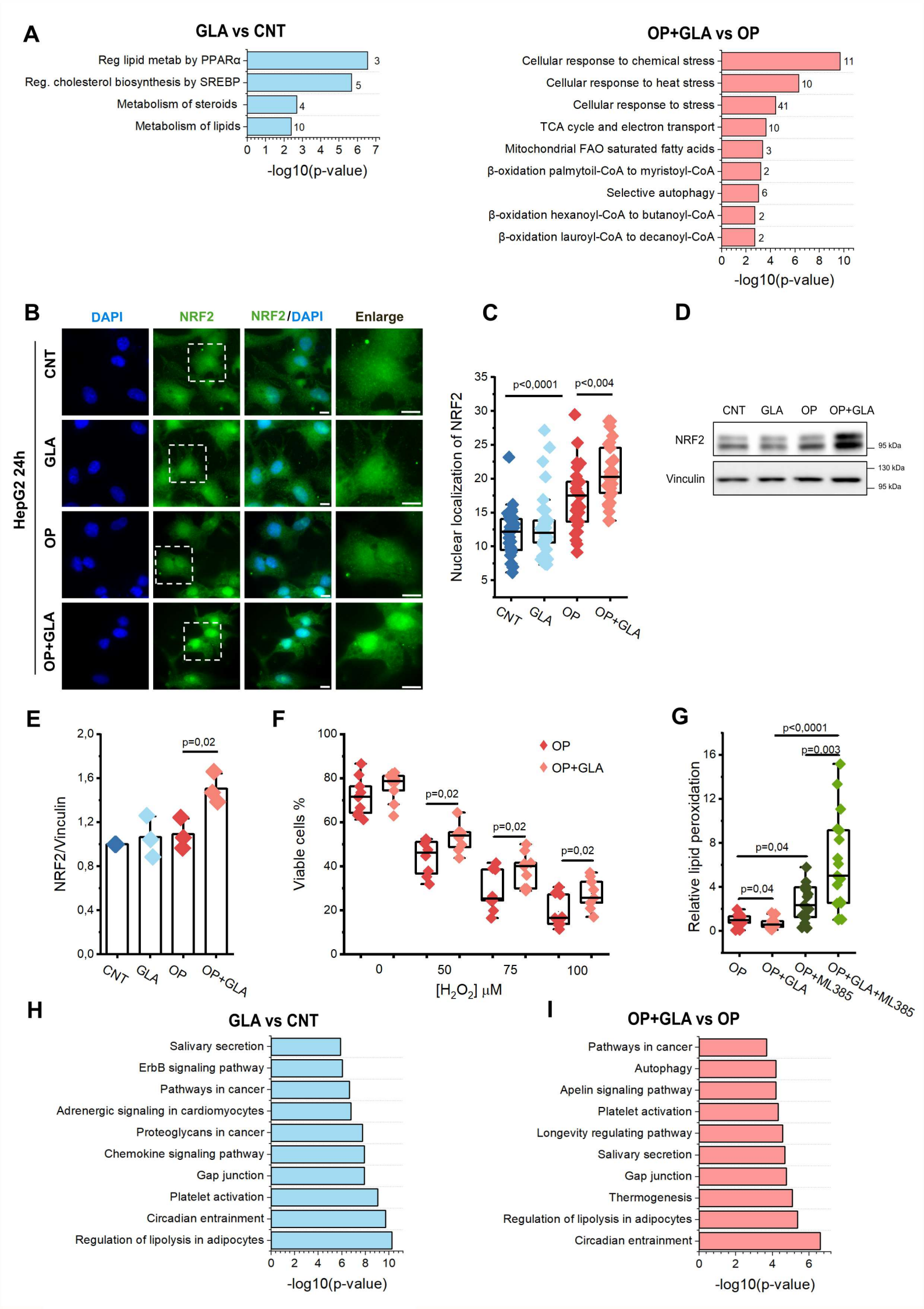
(C-D) Quantification of the number (B) and volume (C) of LDs per cell. Significance was determined by unpaired Student's t-test (n=5).

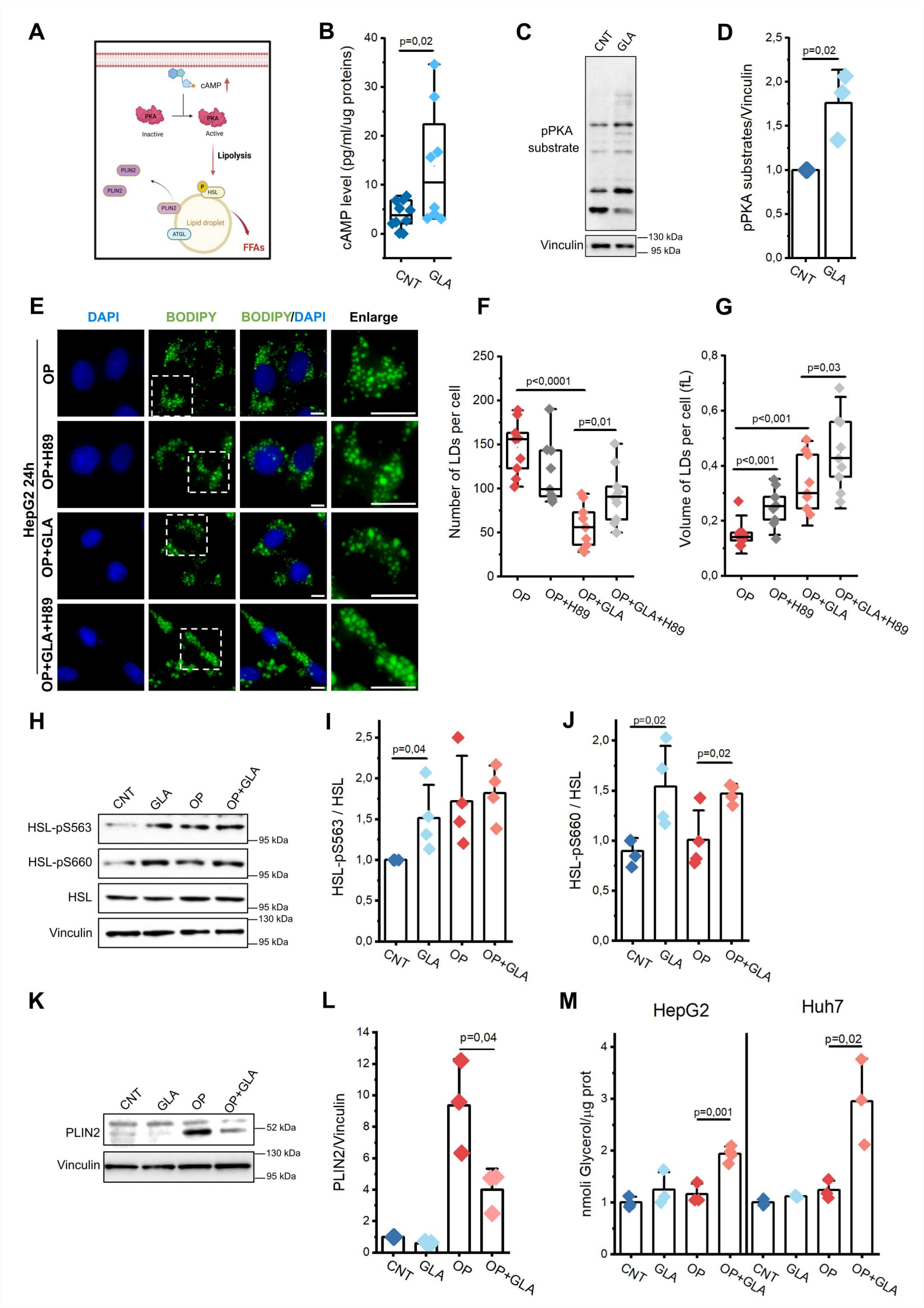
(E) Locomotor performance of flies maintained on a control diet (CNT) or high-fat diet (FD), with or without GLA supplementation, assessed by climbing assay after 3 days of treatment (T1). Curves show the cumulative percentage of flies reaching the predefined climbing height over 120 s; shaded areas represent the SEM. Statistical analysis was performed on AUC values calculated for each independent vial using the trapezoidal method. AUC values from T0 and T1 were analyzed by two-way repeated-measures ANOVA, followed by Tukey's multiple-comparisons test for pairwise comparisons among experimental groups at T1. FD+GLA vs FD, adjusted $p = 0.0321$; GLA vs FD, adjusted $p = 0.0129$; CNT vs FD, adjusted $p = 0.0610$ (ns).

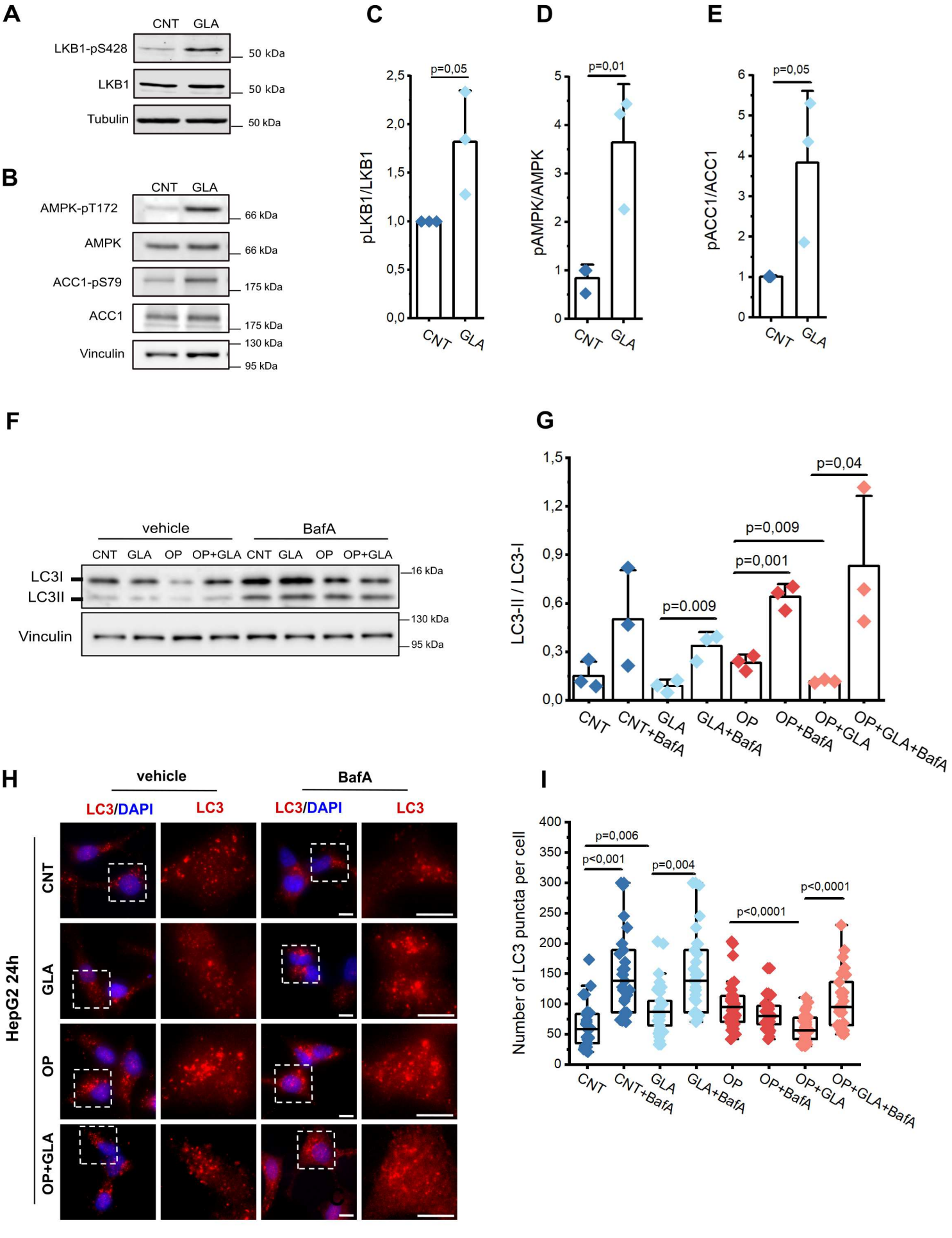
(F) Kaplan-Meier survival curves of male flies maintained on a high-fat diet (FD) in the absence or presence of GLA supplementation (FD+GLA) for 15 days. Curves are shown with 95% confidence intervals (FD, n = 50; FD+GLA, n = 49; five vials per group). Differences in survival distribution were assessed using the log-rank (Mantel-Cox) test ($\chi^2 = 5.39$, $p = 0.0203$).

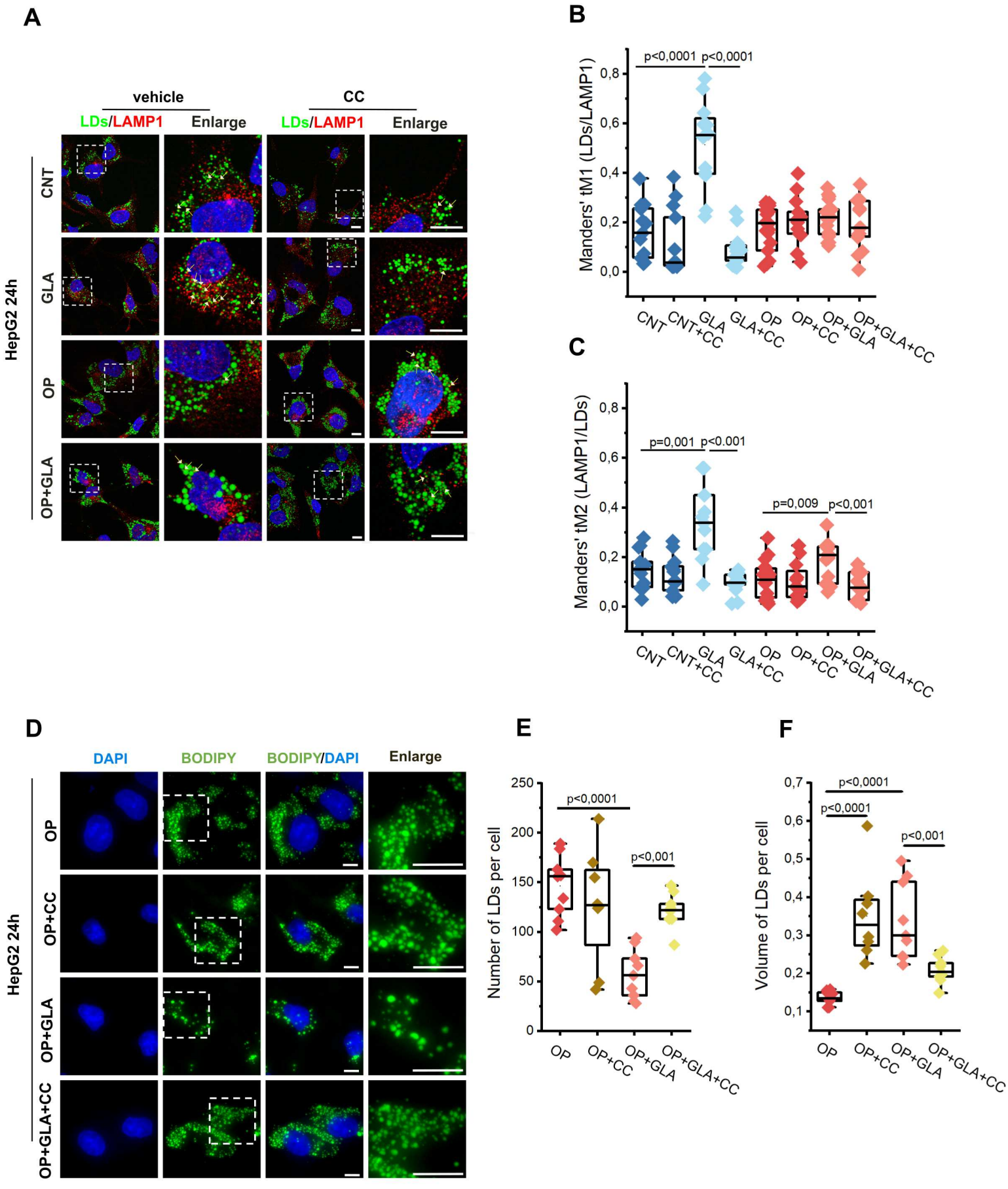
Figure 8. Schematic representation of the proposed molecular mechanism of action of glabranin on the PKA-AMPK axis. Glabranin increases intracellular cAMP levels, triggering PKA activation. Active PKA directly stimulates lipolysis through HSL phosphorylation and activates the LKB1/AMPK signaling pathway. Downstream AMPK activation promotes lipophagy. Fatty acids released through these catabolic processes are directed to mitochondria for β-oxidation. Concurrently, glabranin promotes NRF2 nuclear translocation to enhance the cellular stress response, mitigating ROS generation and lipid peroxidation. Abbreviations: ER, endoplasmic reticulum; FAs, fatty acids; HSL, hormone-sensitive lipase; ATGL, adipose triglyceride lipase; PLIN2, perilipin 2; CPT1/2, carnitine palmitoyltransferase 1/2; ROS, reactive oxygen species. Created with BioRender.com.

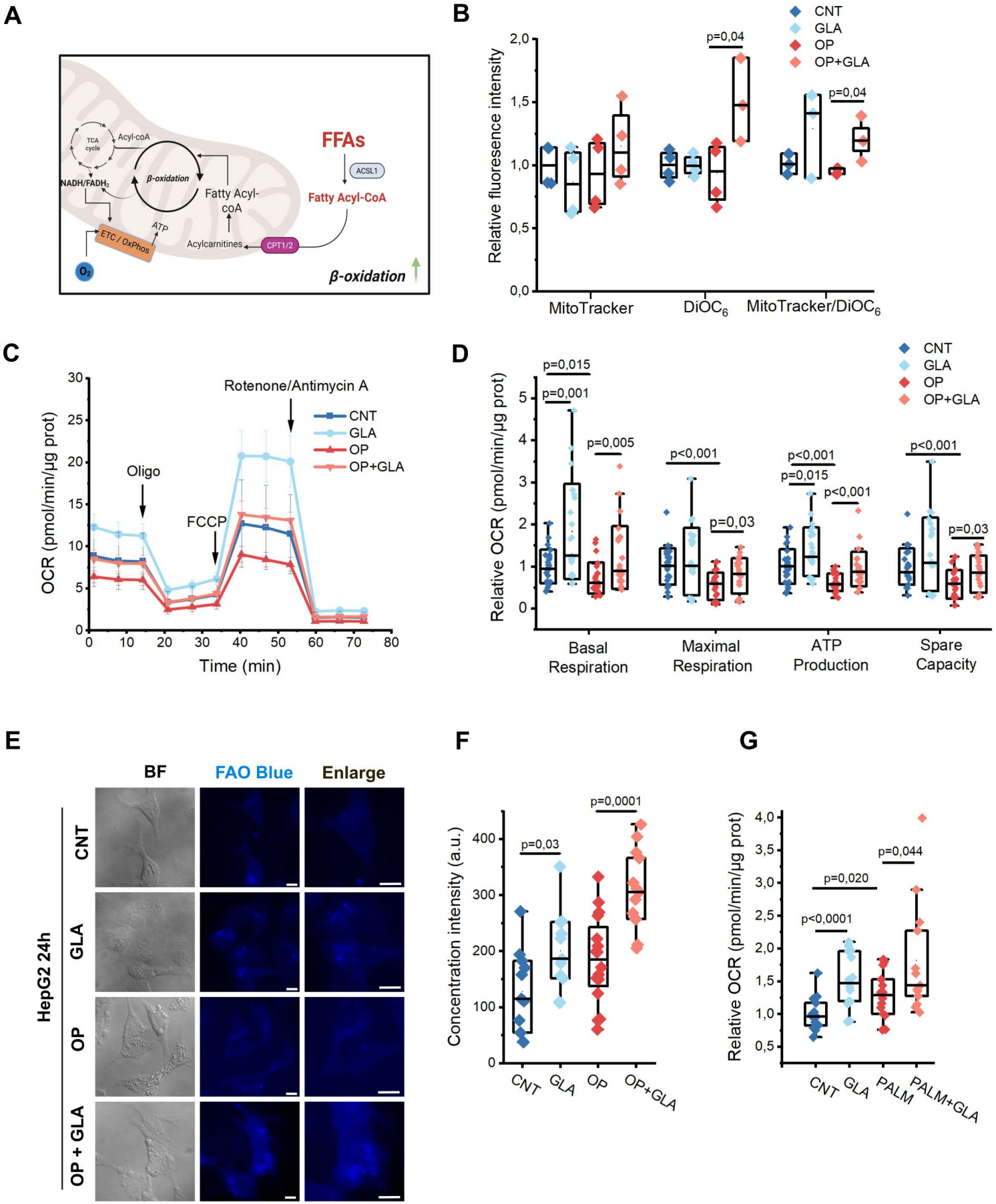

A
Glabranin
Pinocembrin
Licoflavanone
B
HepG2 24h
DAPI
BODIPY
BODIPY/DAPI
Enlarge
CNT
GLA
PINO
LICO
OP
OP+GLA
OP+PINO
OP+LICO
C
Number of LDs per cell
p=0,003
p<0,001
p<0,0001
p=0,02
p<0,0001
p<0,0001
CNT
GLA
LICO
PINO
OP
OP+GLA
OP+LICO
OP+PINO
D
Volume of LDs per cell
p<0,001
p<0,001
p=0,007
p<0,0001
p=0,005
E
Viable cells %
p=0,01
p=0,03
[GLA] (μM)
F
Glabranin (pmol/cell)
Time (h)
G
Relative LDs level
p=0,01

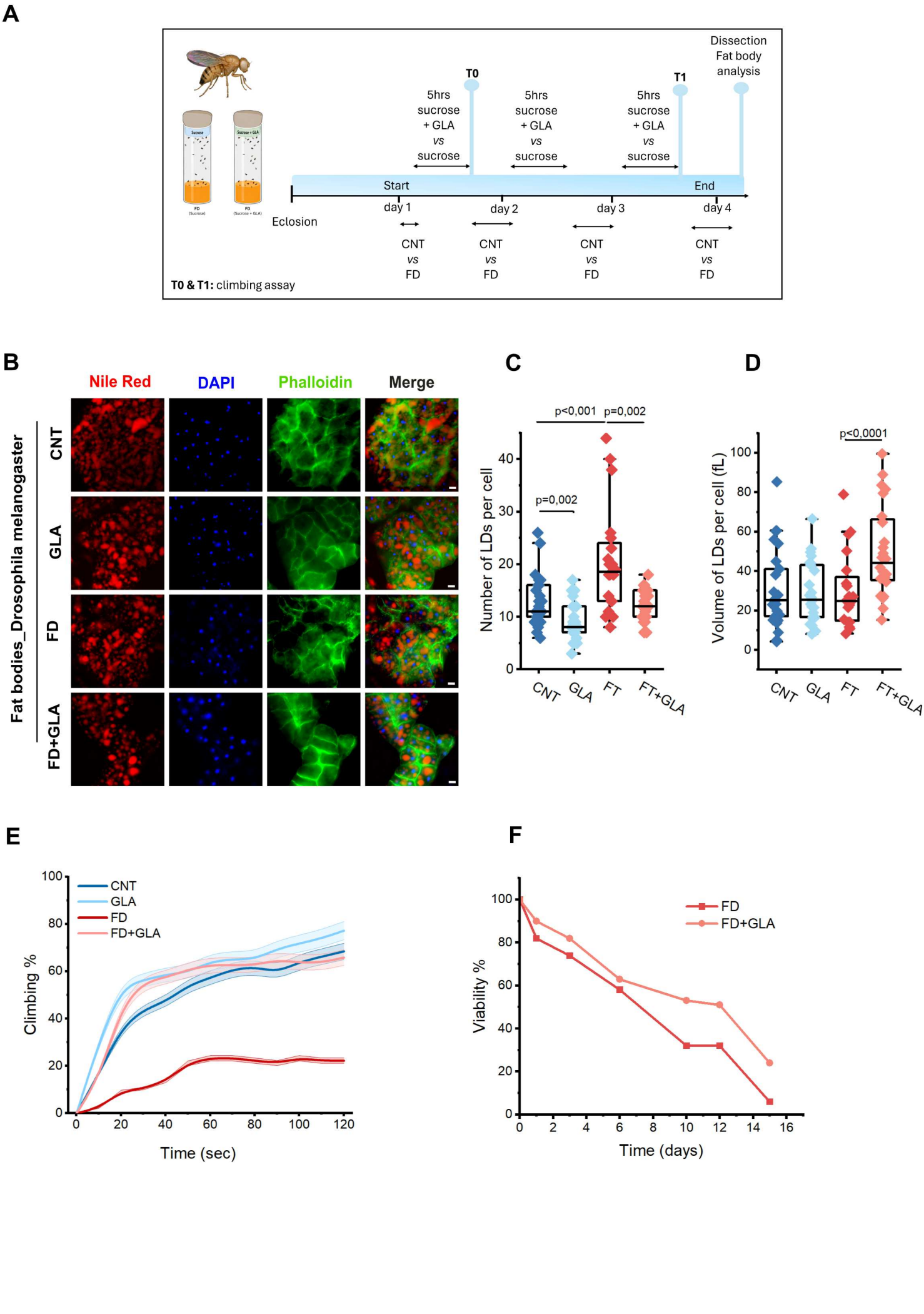

A
GLA vs CNT
Reg lipid metab by PPARα
Reg. cholesterol biosynthesis by SREBP
Metabolism of steroids
Metabolism of lipids
3
5
4
10
0 1 2 3 4 5 6 7
-log10(p-value)
OP+GLA vs OP
Cellular response to chemical stress
Cellular response to heat stress
Cellular response to stress
TCA cycle and electron transport
Mitochondrial FAO saturated fatty acids
β-oxidation palmytoil-CoA to myristoyl-CoA
Selective autophagy
β-oxidation hexanoyl-CoA to butanoyl-CoA
β-oxidation lauroyl-CoA to decanoyl-CoA
11
10
41
10
3
2
6
2
2
0 2 4 6 8 10
-log10(p-value)
B
DAPI
NRF2
NRF2/DAPI
Enlarge
HepG2 24h
CNT
GLA
OP
OP+GLA
C
p<0,0001
p<0,004
Nuclear localization of NRF2
CNT
GLA
OP
OP+GLA
D
CNT
GLA
OP
OP+GLA
NRF2
Vinculin
95 kDa
130 kDa
95 kDa
E
p=0,02
NRF2/Vinculin
CNT
GLA
OP
OP+GLA
F
OP
OP+GLA
p=0,02
p=0,02
p=0,02
Viable cells %
[H2O2] µM
G
p<0,0001
p=0,003
p=0,04
p=0,04
Relative lipid peroxidation
OP
OP+GLA
OP+ML385
OP+GLA+ML385
H
GLA vs CNT
Salivary secretion
ErbB signaling pathway
Pathways in cancer
Adrenergic signaling in cardiomyocytes
Proteoglycans in cancer
Chemokine signaling pathway
Gap junction
Platelet activation
Circadian entrainment
Regulation of lipolysis in adipocytes
0 2 4 6 8 10
-log10(p-value)
I
OP+GLA vs OP
Pathways in cancer
Autophagy
Apelin signaling pathway
Platelet activation
Longevity regulating pathway
Salivary secretion
Gap junction
Thermogenesis
Regulation of lipolysis in adipocytes
Circadian entrainment
0 2 4 6
-log10(p-value)

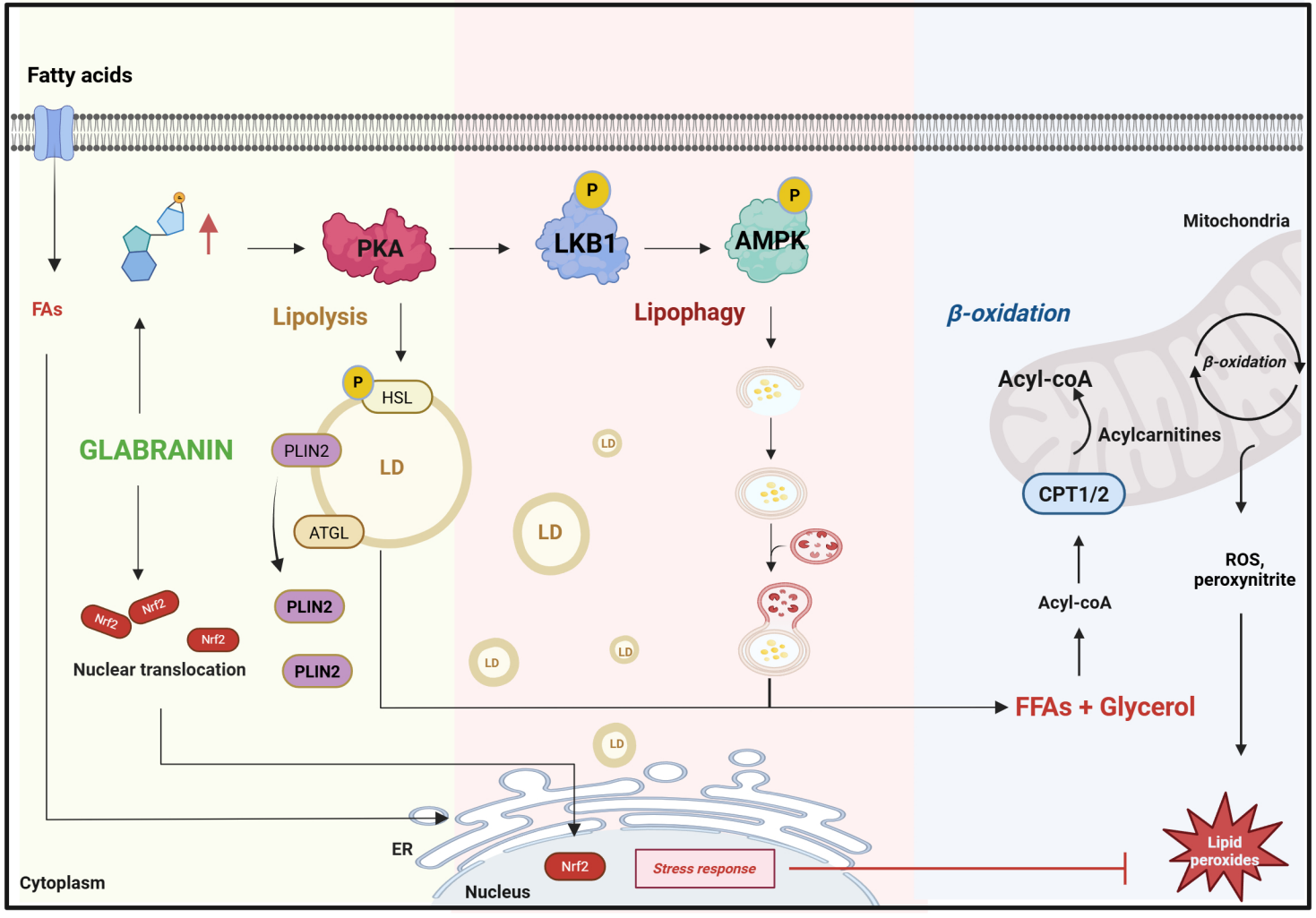

A
cAMP
PKA
Inactive
PKA
Active
Lipolysis
PLIN2
PLIN2
PLIN2
P
HSL
Lipid droplet
ATGL
FFAs
B
p=0,02
cAMP level (pg/ml/ug proteins)
CNT
GLA
C
CNT
GLA
pPKA substrate
Vinculin
130 kDa
95 kDa
D
p=0,02
pPKA substrates/Vinculin
CNT
GLA
E
DAPI
BODIPY
BODIPY/DAPI
Enlarge
HepG2 24h
OP
OP+H89
OP+GLA
OP+GLA+H89
F
p<0,0001
p=0,01
Number of LDs per cell
OP
OP+H89
OP+GLA
OP+GLA+H89
G
p=0,03
p<0,001
p<0,001
Volume of LDs per cell (fL)
OP
OP+H89
OP+GLA
OP+GLA+H89
H
CNT
GLA
OP
OP+GLA
HSL-pS563
HSL-pS660
HSL
Vinculin
95 kDa
95 kDa
95 kDa
130 kDa
95 kDa
I
p=0,04
HSL-pS563 / HSL
CNT
GLA
OP
OP+GLA
J
p=0,02
p=0,02
HSL-pS660 / HSL
CNT
GLA
OP
OP+GLA
K
CNT
GLA
OP
OP+GLA
PLIN2
Vinculin
52 kDa
130 kDa
95 kDa
L
p=0,04
PLIN2/Vinculin
CNT
GLA
OP
OP+GLA
M
HepG2
Huh7
p=0,001
p=0,02
nmoli Glycerol/µg prot
CNT
GLA
OP
OP+GLA
CNT
GLA
OP
OP+GLA


A
CNT GLA
LKB1-pS428
50 kDa
LKB1
50 kDa
Tubulin
50 kDa
B
CNT GLA
AMPK-pT172
66 kDa
AMPK
66 kDa
ACC1-pS79
175 kDa
ACC1
175 kDa
Vinculin
130 kDa
95 kDa
C
pLKB1/LKB1
p=0,05
CNT GLA
D
pAMPK/AMPK
p=0,01
CNT GLA
E
pACC1/ACC1
p=0,05
CNT GLA
F
vehicle
BafA
CNT GLA OP OP+GLA CNT GLA OP OP+GLA
LC3I
LC3II
16 kDa
Vinculin
130 kDa
95 kDa
G
LC3-II / LC3-I
p=0,04
p=0,009
p=0,001
p=0.009
CNT CNT+BafA GLA GLA+BafA OP OP+BafA OP+GLA OP+GLA+BafA
H
vehicle
BafA
LC3/DAPI
LC3
LC3/DAPI
LC3
HepG2 24h
CNT
GLA
OP
OP+GLA
I
Number of LC3 puncta per cell
p=0,006
p<0,001
p=0,004
p<0,0001
p<0,0001
CNT CNT+BafA GLA GLA+BafA OP OP+BafA OP+GLA OP+GLA+BafA


A
vehicle
CC
LDs/LAMP1
Enlarge
LDs/LAMP1
Enlarge
HepG2 24h
CNT
GLA
OP
OP+GLA
B
Manders' tM1 (LDs/LAMP1)
p<0,0001
p<0,0001
0,0
0,2
0,4
0,6
0,8
CNT
CNT+CC
GLA
GLA+CC
OP
OP+CC
OP+GLA
OP+GLA+CC
C
Manders' tM2 (LAMP1/LDs)
p=0,001
p<0.001
p=0,009
p<0,001
0,0
0,2
0,4
0,6
0,8
CNT
CNT+CC
GLA
GLA+CC
OP
OP+CC
OP+GLA
OP+GLA+CC
D
DAPI
BODIPY
BODIPY/DAPI
Enlarge
HepG2 24h
OP
OP+CC
OP+GLA
OP+GLA+CC
E
Number of LDs per cell
p<0,0001
p<0,001
0
50
100
150
200
250
OP
OP+CC
OP+GLA
OP+GLA+CC
F
Volume of LDs per cell
p<0,0001
p<0,0001
p<0,001
0,1
0,2
0,3
0,4
0,5
0,6
0,7
OP
OP+CC
OP+GLA
OP+GLA+CC


A
TCA cycle
Acyl-coA
NADH/FADH2
β-oxidation
Fatty Acyl-coA
ATP
ETC / OxPhos
O2
Acylcarnitines
CPT1/2
FFAs
ACSL1
Fatty Acyl-CoA
β-oxidation
B
CNT
GLA
OP
OP+GLA
Relative fluoresence intensity
p=0,04
p=0,04
MitoTracker
DiOC6
MitoTracker/DiOC6
C
Rotenone/Antimycin A
Oligo
FCCP
OCR (pmol/min/µg prot)
Time (min)
D
p=0,015
p=0,001
p=0,005
p<0,001
p=0,03
p<0,001
p=0,015
p<0,001
p<0,001
p=0,03
Relative OCR (pmol/min/µg prot)
Basal Respiration
Maximal Respiration
ATP Production
Spare Capacity
E
BF
FAO Blue
Enlarge
HepG2 24h
CNT
GLA
OP
OP + GLA
F
p=0,03
p=0,0001
Concentration intensity (a.u.)
CNT
GLA
OP
OP+GLA
G
p<0,0001
p=0,020
p=0,044
Relative OCR (pmol/min/µg prot)
CNT
GLA
PALM
PALM+GLA


A
Dissection
Fat body
analysis
T0
T1
5hrs
sucrose
+ GLA
vs
sucrose
5hrs
sucrose
+ GLA
vs
sucrose
5hrs
sucrose
+ GLA
vs
sucrose
Start
End
Eclosion
day 1
day 2
day 3
day 4
CNT
vs
FD
CNT
vs
FD
CNT
vs
FD
CNT
vs
FD
T0 & T1: climbing assay
B
Nile Red
DAPI
Phalloidin
Merge
Fat bodies_Drosophila melanogaster
CNT
GLA
FD
FD+GLA
C
p<0,001
p=0,002
p=0,002
Number of LDs per cell
CNT
GLA
FT
FT+GLA
D
p<0,0001
Volume of LDs per cell (fL)
CNT
GLA
FT
FT+GLA
E
CNT
GLA
FD
FD+GLA
Climbing %
Time (sec)
F
FD
FD+GLA
Viability %
Time (days)


Fatty acids
FAs
PKA
LKB1
AMPK
P
Mitochondria
Lipolysis
Lipophagy
β-oxidation
GLABRANIN
HSL
PLIN2
LD
ATGL
Acyl-coA
β-oxidation
Acylcarnitines
CPT1/2
Nrf2
Nuclear translocation
ROS,
peroxynitrite
Acyl-coA
FFAs + Glycerol
ER
Nucleus
Stress response
Lipid
peroxides
Cytoplasm